Computer Methods in Applied Mechanics and Engineering 455 (2026) 118927

Contents lists available at ScienceDirect

Comput. Methods Appl. Mech. Engrg.

journal homepage: www.elsevier.com/locate/cma

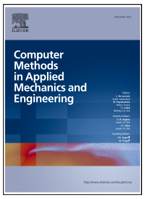

In vivo blood viscosity estimation from microscopic images by solving an inverse incompressible Navier-Stokes problem

Shota Ito [a,b,*], Moritz Vogel [c], Adrian A. Fessler [c], Adrian Kummerländer [a,c], Anna Lischke [d], Dietmar Gradl [d], Ferdinand le Noble [d], Mathias J. Krause [a,b,c], Stephan Simonis [a,c]

[a] *Lattice Boltzmann Research Group, Karlsruhe Institute of Technology, Germany*
[b] *Institute of Mechanical Process Engineering and Mechanics, Karlsruhe Institute of Technology, Germany*
[c] *Institute for Applied and Numerical Mathematics, Karlsruhe Institute of Technology, Germany*
[d] *Department of Cell and Developmental Biology, Zoological Institute, Karlsruhe Institute of Technology, Germany*

ARTICLE INFO

Keywords:
Microscopic imaging
Computational fluid dynamics
Inverse problems
Hemodynamics

ABSTRACT

Reliable routines for assessing in vivo blood viscosity is an ongoing challenge. This limits bedside monitoring, cardiovascular risk stratification, and the parameterization of patient-specific computational hemodynamic models. While inverse modeling approaches have been explored in the biomedical field extensively, the feasibility of estimating effective blood viscosity remains insufficiently investigated, wherein many existing methods rely on simplified flow descriptions and have rarely been applied to real measurement data. In this work, we present a non-invasive framework that combines microvascular particle image velocimetry (micro-PIV) with computational fluid dynamics (CFD) to estimate the effective blood viscosity in vivo. Time-averaged velocity fields are reconstructed from high-speed microscopic image sequences of blood flow, using red blood cells as tracer particles. These velocity fields are incorporated into an inverse formulation of the incompressible Navier-Stokes equations for an either Newtonian or non-Newtonian fluid, which is solved using full CFD simulations. The proposed approach is validated using synthetic benchmark cases with varying noise intensity and vessel geometries, demonstrating robust recovery of power-law viscosity parameters. As a proof of concept, the framework is applied to in vivo microcirculatory data obtained from zebrafish embryos, yielding effective viscosity estimates consistent with values reported in the literature. The presented method establishes an image-based, physics-constrained framework for estimating blood rheology and provides a tool to improve the parameterization and validation of computational hemodynamic models.

1. Introduction

Cardiovascular diseases (CVD) such as heart infarction and stroke are the leading causes of death and contribute substantially to healthcare costs in Western societies [1,2]. A major underlying cause of these events is atherosclerosis, which significantly alters local hemodynamics [3]. In particular, changes in blood viscosity and shear-dependent flow behavior play a crucial role in plaque progression, thrombus formation, and the risk of vessel occlusion [4,5].

---

[*] Corresponding author.
E-mail address: shota.ito@kit.edu (S. Ito).

https://doi.org/10.1016/j.cma.2026.118927
Received 28 January 2026; Received in revised form 13 March 2026; Accepted 13 March 2026

Although several studies have demonstrated correlations between blood viscosity and CVD [3,4,6–8], its role in routine medical diagnostics is largely underestimated in risk stratification and prevention. In perfused vascular networks, blood viscosity is a principal component of frictional shear forces exerted on blood vessels and vascular resistance to blood flow. Blood viscosity refers to the total viscosity of the particulate suspension of blood plasma and blood cells, encompassing the physical properties of red blood cells (RBCs), such as deformability and RBC aggregation, as well as plasma factors, including protein content [9]. Elevated blood viscosity increases peripheral resistance and augmented shear stress levels, adversely affecting tissue perfusion, and raises the risk for endothelial cell damage, and thromboembolic events [7,8,10,11].

While the importance of blood viscosity for human cardiovascular pathology and for hemodilution strategies in the intensive care unit is widely recognized, routine, non-invasive measurements in discrete sections of the vascular tree are not possible, thereby limiting bedside monitoring, risk stratification, and clinical decision-making. Blood viscosity is typically measured ex vivo using a shear or capillary rheometer [12,13]. However, this approach requires invasive blood sampling, which may alter the effective viscosity through activating the coagulation cascade and immune response. Furthermore, blood viscosity strongly depends on the local hematocrit, as it is not homogeneously distributed in the micro-circulation, thereby limiting the comparability of in vivo and ex vivo measurements [14,15]. Finally, the technical complexity and the time-intensive nature limit the practical applicability of this technique, making the reliable assessment of blood viscosity clinically challenging.

Recent advances in computational fluid dynamics (CFD) applied to hemodynamics provide an alternative approach to experiments to predict and understand the behavior of circulatory blood flow in the human body [16–18]. Applications range from optimizing medical device design, such as stents, valve prostheses, and ventricular assist devices, to the detailed characterization of complex physiological pressure and flow fields and the computation of metrics which cannot be directly measured, e.g., the wall shear stress [16,17]. At the macroscopic level (vessel diameters above 300 μm), non-Newtonian viscosity models such as power-law, Carreau-Yasuda, or Casson model are commonly applied to approximate the shear-thinning behavior of blood [14,18]. In smaller vessels, particulate effects become dominant such that the individual RBCs are fully resolved using coupled numerical solvers for the structural mechanics for the immersed membrane and fluid dynamics for the surrounding plasma [19,20].

One challenge in the field of computational hemodynamics is the appropriate parameterization of the viscosity models on both macroscopic and microscopic scales [6]. This issue becomes even more pressing for accurate patient-specific numerical investigations. At the microscale, several relevant model parameters are currently simply not measurable, such as the RBC membrane stiffness or the parametrization of cell-cell interaction forces [19,21]. This results in assumptions and simplifications while performing the numerical simulation, e.g., many numerical studies assume blood as a Newtonian fluid, thereby neglecting shear-rate dependent effects [6,22]. Together with the experimental side, the general challenges which we aim to address in the presented work are: first, the lack of established in vivo approaches for blood viscosity assessment, and second, the resulting difficulty in parameterizing computational hemodynamic models for patient-specific investigations.

A promising approach to address these gaps is the use of inverse problems, which have gained attraction and rapidly expanded their application due to the increased availability of clinical data [6]. Rather than setting up a simulation with *a priori* knowledge of parameters and then validating the results with experimental results, inverse problems aim to identify unknown parameters iteratively by minimizing the deviation between the numerical results and measurement data. Inverse problems are widely applied in biomedical problems, e.g., for reconstructing unknown or inaccurate boundary conditions in simulations, estimating difficult to measure or simply unknown model parameters, and improving measurement data quality by combining with CFD methods. Adib *et al.* [23] reconstructed unknown outflow pressure conditions from velocity distributions obtained from phase-contrast magnetic resonance images (PC-MRI) in hemodynamic simulations. Funke *et al.* [24] simultaneously estimate time-varying velocity boundary conditions and the uncertain initial condition from velocity measurements. Therein, as a proof-of-concept, they applied their approach to a real 3D aneurysm using 4D Flow ex vivo measurements of a dog's vessel using 4D PC-MRI data and reported limitations on the grid resolution in the numerical simulation due to computational expenses [6,24]. Further, Koltukluo *et al.* [25] solved boundary control problems for hemodynamic flows based on MRI measurements. Arthurs *et al.* [26] approximated boundary model parameters in reduced-order models for the full time-dependent Navier-Stokes model with simplified fluid-structure interaction (FSI) effects on the wall. As the input for the inverse problem, flow rates from 2D PC-MRI and pressure forms obtained by applanation tonometry in the carotid are used in aortas with synthetic and subject's data. Parameter estimation problems formulated in a least-squares fashion generally exhibit higher robustness regarding the uncertainty in the input data due to its overdetermined nature compared to distributed control problems, as in [23] and [24]. Perego *et al.* [27] investigated the compliance of the cardiovascular tissue by estimating the Young's modulus of arterial wall stiffness from displacement measurements at the fluid-solid interface. Klemens *et al.* [28,29] addressed inverse problems based on incompressible Navier-Stokes models to improve MRI image quality by suppressing noise signals utilizing CFD and gradient-based optimization methods. Kontogiannis *et al.* [30] addressed a joint inverse flow problem, where they reconstructed the flow field and boundary parameters from MRI velocity data.

To the author's knowledge, only limited studies addressed the inverse determination of the blood viscosity. Larson *et al.* [31] executed the first attempt on the inverse determination of blood viscosity in the context of detecting arterial wall abnormalities. They used Bayesian optimization with uncertainty quantification for 1D networks for a bifurcating arterial network, where noisy, synthetic velocity data is fed into the framework to estimate blood viscosity, arterial stiffness, and vessel area. Habibi *et al.* [32] identified unknown boundary conditions and the viscosity for a Newtonian fluid model using synthetic CFD data for various hemodynamic benchmark cases, such as the idealized aneurysm model. Based on the conducted literature review, the following two challenges in inverse determination of the blood viscosity are identified: the non-uniqueness of the parameter solution due to ill-posedness of the problem formulation, and the limitation on computational resources when including real 3D measurement data. In the above studies, no real measurement data is included, leaving the influence of the uncertainty in the input data due to noise signals insufficiently

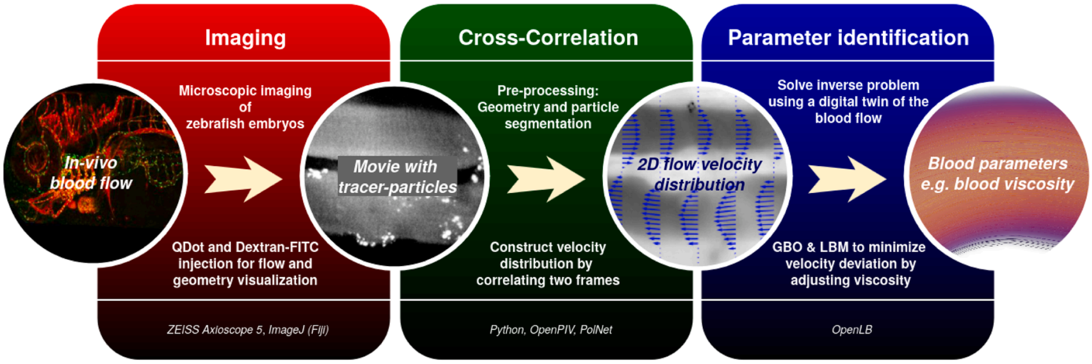

Fig. 1. Complete PIV-iCFD workflow.

explored. Furthermore, both studies stated that the governing flow equations are not enforced, as no full CFD simulations are conducted due to demanding computational resources, and assumed the fluid model to be a Newtonian model, neglecting shear-dependent effects arising from RBC deformability. Kontogiannis *et al.* [33] recovered viscosity model parameters for the Carreau model by combining Bayesian optimization, CFD simulations, and MRI velocity measurements for the US Food and Drug Administration's benchmark nozzle. They demonstrated that the Carreau parameters obtained from the flow-MRI data alone are in very good agreement with the parameters learned from the experimental data.

In this paper, we propose a novel non-invasive method for identifying in vivo blood viscosity based on optical imaging of microvascular blood flow and particle image velocimetry (PIV) by solving an inverse incompressible Navier-Stokes problem (which we refer to as PIV-iCFD, for PIV and inverse CFD). The inverse problem is fed with time-averaged velocity distributions obtained by averaging distributions computed by cross-correlating the gray values of frame pixels in two consecutive frames based on PIV, wherein the RBCs act as tracer particles as in [34]. Previous studies have shown that the usage of spatially distributed input data provides robustness in inverse problems even for a relatively low signal-to-noise ratio, which motivates the choice of PIV in our method [35,36]. Based on the reconstructed velocity distributions, the algorithm solves the inverse problem by combining gradient-based optimization with CFD simulations with exchangeable models for Newtonian or non-Newtonian fluids to deliver blood dynamics characteristics such as viscosity. For the discretization of the governing hydrodynamic flow equations, the lattice Boltzmann method (LBM) is used, which gained popularity as an efficient scheme with great suitability for biomedical applications with complex geometries and its capability to saturate high-performance computing resources due to its algorithmic structure [37]. The numerical efficiency of LBM is crucial here to address iterative optimization problems, such as in inverse problems, as previously shown in [35]. The proposed approach is validated using synthetic benchmark cases for Newtonian and non-Newtonian fluids with varying configurations regarding noise intensity, vessel geometry, and flow rates. As a proof-of-concept, the framework is applied on in vivo circulatory flow in a set of zebrafish embryos to estimate the effective viscosity. The novelty addressed in the presented manuscript is as follows:

- the influence of different synthetic configurations regarding the vessel geometry, noise signal intensity, and flow rate on the inverse estimation of the viscosity,
- the impact of non-Newtonian viscosity models (power-law fluids) compared to Newtonian models on the inverse problem formulation,
- a feasibility study of using cross-correlated velocity distributions based on micro-PIV as input data for the inverse problem
- a proof-of-concept of the presented approach using real PIV velocity sets from micro-circulation in zebrafish embryos to assess the effective blood viscosity

This work explicitly solves full CFD simulations using the efficient LBM discretization, thereby enforcing the governing hydrodynamic flow equations, as this approach showed to be promising in the literature [25,30,33]. Therefore, the admissible solutions for the inverse problems are restricted to solutions of the physical equations, limiting the solution space of the inverse problem, as previously shown in [35].

The remainder of this paper is structured as follows. Section 2 describes the proposed PIV-iCFD approach and its individual substeps of the complete workflow, i.e., microscopic imaging, cross-correlation, and parameter identification. Section 3 presents and discusses the validation results and the application to in vivo zebrafish data. Finally, Section 4 concludes the paper with a summary of key findings and suggests future research directions.

2. Methodology: PIV-iCFD

We propose a novel approach for assessing blood viscosity in vivo, named PIV-iCFD, which consists of three steps: imaging, cross-correlation, and parameter identification process. Briefly, this method aims to identify viscosity model parameters, where first velocity profiles are computed based on the same technique as PIV, where the erythrocytes or injected tracer particles in blood flow

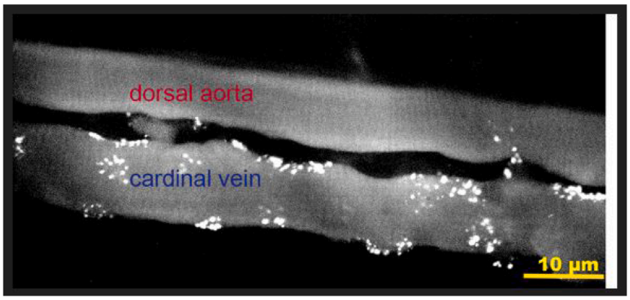

Fig. 2. Merge of five z-stacks of a representative 3 dpf zebrafish embryo to determine the geometry of the dorsal aorta and the cardinal vein.

images are correlated frame-wise. Then, an inverse problem is solved, where the viscosity model parameters are identified from the computed velocity distribution using CFD simulations. The entire workflow with the interfaces is sketched in Fig. 1.

In the first step, an animation of blood circulation is recorded by taking microscopic images of experimental models (zebrafish embryos) in vivo. The captured targets are arterial and venous vessel sections with different flow rates along the vessel diameter, where, for the inverse problem, only the venous region is used due to lower pulsation effects. Either existing erythrocytes or injected nanoparticles act as tracer particles that will be used for cross-correlation in the next step. The movement of the tracer particles recorded on the frames is then cross-correlated frame-wise to obtain a two-dimensional velocity profile of the blood flow. In this step, additionally, the vessel geometry in the images is segmented to create a three-dimensional surface model, which is later used in flow simulations. This is done based on automated centerline detection followed by radial extrusion to obtain a triangulated approximation of the vessel surface [38]. Finally, the computed velocity distribution and extracted vessel surface model are used to construct a digital twin of the imaged blood flow setup, which is used to solve an inverse Navier-Stokes problem to identify blood viscosity model parameters. A gradient-based optimizer minimizes the distance between the input velocity profiles and the simulated profiles by iteratively adjusting the parameter values of the applied viscosity model (e.g., Newtonian, non-Newtonian as power-law fluids). For efficient solving of the hydrodynamic equations, the LBM is used as the discretization scheme, where the required gradients are computed via automatic differentiation. Several existing software packages are utilized for the workflow. That is, *OpenPIV* [39] for the cross-correlation, *PolNet* [38] for the geometry model segmentation, and *OpenLB* [40] for the flow simulation and solving of the inverse problem.

In the following subsections, the methodology utilized in each step of Fig. 1 is explained.

2.1. Microscopic imaging

Zebrafish larvae were embedded in 0.5% (w/v) low-melting agarose (NuSieve GTG Agarose, Lonza) in 35 mm glass bottom microscopy dishes (MatTek). The agarose was covered with E3 medium and 0.003% (w/v) PTU (Sigma). To prevent movement of the embryo during in vivo recordings, the E3 medium was supplemented with 0.112 mg ml^{-1} Tricaine. In vivo images were acquired using a Zeiss Axioscope-5, equipped with Colibri-3 fluorescence LED illumination unit, Zeiss EC Plan NeoFluar 10x/0.3 objective, AxioCam 702 monochrome camera, and recorded using Zeiss ZEN-3.1 image acquisition software running under Windows 10 Pro. To image blood flow in three days post fertilization (3dpf) wildtype embryos, a 0.5μm solution containing Texas-Red Dextran 70kDa for visualization of the blood plasma and vessel dimensions were injected into the blood stream, as shown in Fig. 2. Trunk vessels were imaged at the level of the yolk-sac elongation.

2.2. Velocity distribution construction via cross-correlation

To construct the velocity distribution from the taken microscopic images, the technique of PIV is applied. The aim is to compute a velocity distribution throughout the image using cross-correlation on two consecutive frames at $t = t_1$ and $t = t_1 + \triangle t_{\mathrm{PIV}}$ with $\triangle t_{\mathrm{PIV}}$ the frame duration. Each image is divided into multiple smaller equally sized windows, referred to as interrogation volumes (IV), where for every one IV a single approximation for the averaged velocity will be computed. To perform cross-correlation, for each IV, a second window in the frame at $t = t_1 + \triangle t_{\mathrm{PIV}}$, referred to as search volume (SV), is correlated, where each SV is associated with exactly one IV. Let a single frame be of image resolution $r_x \times r_y$, $r_x, r_y \in \mathbb{N}$, and define the notation $[a, b] = \{a \leq i < b \mid i \in \mathbb{N}\}$ as the left-closed and right-open interval over natural numbers with the short form $[n] = [0, n]$. Then, $f : [r_x] \times [r_y] \to \mathbb{R}$ is the mapping of the pixel indices to grayscale image intensity values for the first frame at $t = t_1$ and $g : [r_x] \times [r_y] \to \mathbb{R}$ for the second frame at $t = t_1 + \triangle t_{\mathrm{PIV}}$, respectively. For a single IV, let $\boldsymbol{o}_{\mathrm{IV}} \in \mathbb{N}^2$ be the origin and $\boldsymbol{e}_{\mathrm{IV}} = (i_x, i_y) \in \mathbb{N}^2$ the extent of the IV window, which means that IV covers the pixels with the indices in $\{(a, b) \mid \boldsymbol{o}_{\mathrm{IV},x} \leq i \boldsymbol{o}_{\mathrm{IV},x} + i_x, \boldsymbol{o}_{\mathrm{IV},y} \leq j \leq \boldsymbol{o}_{\mathrm{IV},y} + i_y\}$. Analogously, define $\boldsymbol{o}_{\mathrm{SV}} \in \mathbb{N}^2$ and $\boldsymbol{e}_{\mathrm{SV}} = (s_x, s_y) \in \mathbb{N}^2$ as the origin and extent of the SV.
The discrete two-dimensional cross-correlation on IV and SV from images f and g is defined as

$$(f \star g)(\boldsymbol{s}) = \sum_{(a,b) \in [i_x] \times [i_y]} f(\boldsymbol{o}_{\mathrm{IV}} + (a, b)) \cdot g(\boldsymbol{o}_{\mathrm{IV}} + (a, b) + \boldsymbol{s}) \tag{1}$$

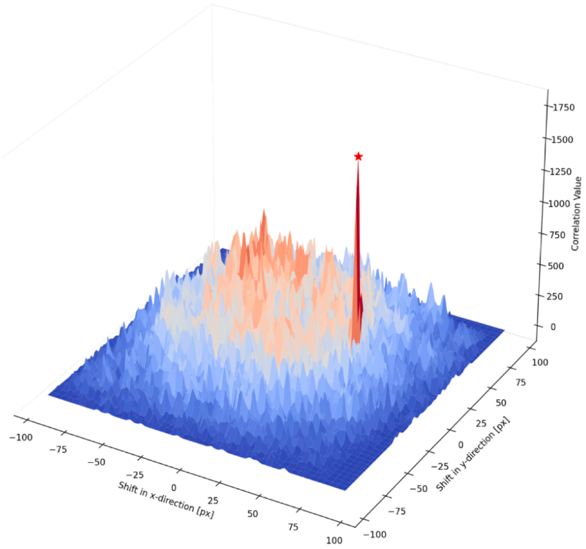

Fig. 3. Exemplary correlation map during cross-correlation.

for a given shift $\boldsymbol{s} \in \mathbb{N}^2$ restricted by $\boldsymbol{s} \in [-s_x/2 + i_x/2, s_x/2 - i_x/2] \times [-s_y/2 + i_y/2, s_y/2 - i_y/2]$ to limit the possible displacement of IV inside the SV. To account for every image intensity value equally, the input functions are normalized as

$$\hat{f} = \frac{f - \mu_f}{\sigma_f}, \tag{2}$$

where μ_f and σ_f are the mean image intensity and standard deviation, respectively. For efficient computation, the multidimensional discrete Fourier transform operator $\mathcal{F}$ with its inverse $\mathcal{F}^{-1}$ and the discrete convolution theorem [41] and symmetry properties are utilized, resulting in the following results.

$$\hat{f} \star \hat{g} = \mathcal{F}^{-1}\left(\overline{\mathcal{F}\hat{f}} \cdot \mathcal{F}\hat{g}\right). \tag{3}$$

Repeating solving (3) for every admissible shift s, the pixel position with the maximum correlation is found, showing the most likely displacement that occurred between the two consecutive frames, as shown in Fig. 3. Performing this for every pair of IV and SV, a two-dimensional velocity distribution is computed, with local velocities calculated via $\boldsymbol{u} = \boldsymbol{s}/\triangle t_{\mathrm{PIV}}$. Further techniques, such as sub-pixel correction, are applied to improve correlation accuracy. Interested readers are referred to [39] for a more detailed explanation of cross-correlation or sub-pixel correction.

2.3. Surface geometry model extraction of blood vessels

To extract surface vessel models for the CFD simulations, *PolNet* [38] is used, an open-source software package based on MatLAB. It is designed for the quantitative analysis of cell polarity and blood flow in vascular networks, particularly in the context of retinal vascular development. The functionality of the software includes the generation of 3D models of blood vessels based on 2D black-and-white images through skeletonization and surface reconstruction, as well as the simulation of blood flow within the generated vessel models. Skeletonization is achieved by extracting the medial axis (centerline) of the vascular network based on a two-dimensional black and white image. Then, with a distance transform, the shortest distance from each lumen pixel to the vessel boundary is calculated, resulting in local radii. For surface reconstruction, a circular cross-section of the vessel is assumed. The resulting skeleton is therefore converted into a 3D volume model in which vessel segments are approximated as cylinders using the local radii. For the CFD simulation of blood flow, the triangulated surface is generated in STL format. Additionally, *PolNet* provides the capability to analyze endothelial cell polarity. The software was specifically developed for flat two-dimensional vascular networks, such as vascular structures in the retina.

2.4. Gradient-based viscosity model parameter identification

In order to obtain the viscosity model parameters $\boldsymbol{\alpha} \in \mathbb{R}^{d_\alpha}$ with the dimension $d_\alpha \in \mathbb{N}$ from the velocity distributions, the following constrained optimization problem is formulated:

$$\begin{aligned} &\text{Minimize} && J(\boldsymbol{\alpha}) = \frac{1}{2}\int_{\Omega^*} (\boldsymbol{u}^* - \mathcal{P}\boldsymbol{u}(\boldsymbol{\alpha}))^2 \mathrm{d}\boldsymbol{x}^*, \\ &\text{while} && \boldsymbol{G}(\boldsymbol{\alpha}) = \left\{ \begin{array}{l} \boldsymbol{\nabla} \cdot \boldsymbol{u}, \\ \frac{\partial \boldsymbol{u}}{\partial t} + \boldsymbol{u} \cdot \boldsymbol{\nabla}\boldsymbol{u} + \boldsymbol{\nabla}\frac{p}{\rho} - \boldsymbol{\nabla} \cdot [\nu(\boldsymbol{\alpha})(\boldsymbol{\nabla}\boldsymbol{u} + \boldsymbol{\nabla}\boldsymbol{u}^{\mathrm{T}})] \end{array} \right. = \boldsymbol{0}, \end{aligned} \tag{4}$$

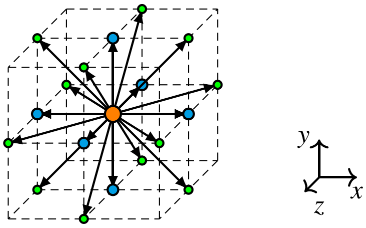

Fig. 4. A schematic illustration of the discrete velocity set $D3Q19$. Coloring refers to energy shells: orange, cyan, and green denote zeroth, first, and second order, respectively. Figure from [45]. (For interpretation of the references to colour in this figure legend, the reader is referred to the web version of this article.)

where p is the pressure and ρ the fluid density. The objective $J : \mathbb{R}^{d_\alpha} \to \mathbb{R}$ computes the distance between the computed velocity distribution from cross-correlation $\boldsymbol{u}^* : \Omega^* \to \mathbb{R}^2$ and the simulated velocity $\boldsymbol{u} : \Omega_{\triangle x} \to \mathbb{R}^3$ projected onto the two-dimensional plane via $\mathcal{P} : \mathbb{R}^3 \to \mathbb{R}^2$ at every discrete position $\boldsymbol{x}^* \in \Omega^*$ where $\boldsymbol{u}^*$ was computed. The constraint $\boldsymbol{G}$ defined in the flow domain Ω gives the continuity equation and the incompressible Navier-Stokes equations (NSE), which are numerically solved for $\boldsymbol{x} \in \Omega_{\triangle x} \subseteq \Omega$ to obtain the velocity distribution $\boldsymbol{u}$. Note that the objective in (4) computes the distance over the velocities averaged in time t to suppress pulsatile effects in the constructed velocities $\boldsymbol{u}^*$ and to simplify the numerical model. Now, for the modeling of the viscosity, different relations between the shear stress and shear rate depending on the desired fluid behavior, different viscosity models can be applied, e.g., for a linear relation, the kinetic viscosity is a scalar $\nu \in \mathbb{R}_{>0}$. It is known that the flow behavior of blood can be modeled as a non-Newtonian fluid on a macroscopic scale [14] as power-law fluids or with the Casson viscosity model. The power-law model gives the apparent kinematic viscosity as

$$\nu(\dot{\gamma}) = \frac{m}{\rho}\dot{\gamma}^{n-1}, \tag{5}$$

where $m \in \mathbb{R}_{>0}$ is the consistency index and $n \in \mathbb{R}$ the power-law index [14]. The optimization problem formulated above presents an inverse problem, namely a parameter identification problem in which the viscosity directly $\boldsymbol{\alpha} = \{\nu\}^{\mathrm{T}}$ or the parameters of the power-law model $\boldsymbol{\alpha} = \{m, n\}^{\mathrm{T}}$ are found by minimizing the deviation between the two velocity fields. The iterative gradient-based optimizer (GBO) LBFGS [42] is used, which is a quasi-Newton method and additional automatized step-size control following the Wolfe rules [43,44] are employed. The constraint $\boldsymbol{G}$ is satisfied by solving $\tilde{\boldsymbol{G}}$, which is a discretized Boltzmann equation that approximates $\boldsymbol{G}$ in the hydrodynamic limit [45]. The required gradients $\mathrm{d}J/\mathrm{d}\boldsymbol{\alpha}$ are obtained by using the forward mode of automatic differentiation [35,46]. The termination condition for optimization is either when the gradient magnitude is below a user-defined threshold or the number of iteration attempts exceeds 50 steps.

2.5. Flow simulation with lattice Boltzmann methods

LBMs are discretization strategies of Boltzmann-type equations that approximate a target equation in the hydrodynamic limit, meaning for vanishing spatial node distances. Typically, the target equation is a system of partial differential equations (PDE) representing a variety of macroscopic transport phenomena such as the Navier-Stokes equation (NSE), advection-diffusion-type equations (ADE), etc. [35,40]. The lattice BGK-Boltzmann equation [47,48] reads

$$f_i(\boldsymbol{x} + \xi_i \triangle t, t + \triangle t) = f_i(\boldsymbol{x}, t) - \frac{\triangle t}{\tau}\left(f_i(\boldsymbol{x}, t) - f_i^{\mathrm{eq}}(\boldsymbol{x}, t)\right), \tag{6}$$

which is solved on each grid position $\boldsymbol{x} \in \Omega_{\triangle x}$ distributed on a homogeneous lattice, on every discrete time step $t \in I_{\triangle t}$ for every i discrete direction according to the $D3Q19$ velocity discretization model as illustrated in Fig. 4. The $DdQq$ notation is established in the LBM community, where d gives the spatial dimension and q the number of discrete velocity directions [49].
In (6), f_i is the particle distribution function (also often referred to as populations), ξ_i the discrete particle velocity, τ the relaxation time, and f_i^{eq} the equilibrium distribution function. The spatial and temporal width of the stencil is given as $\triangle x$ and $\triangle t$, respectively. The equilibrium distribution in (6) is given as

$$f_i^{\mathrm{eq}}(\boldsymbol{x}, t) = w_i \rho \left(1 + \frac{\xi_i \cdot \boldsymbol{u}}{{c_s}^2} + \frac{(\boldsymbol{u} \cdot \xi_i)^2}{2{c_s}^4} - \frac{\boldsymbol{u} \cdot \boldsymbol{u}}{2{c_s}^2}\right), \tag{7}$$

where w_i are the weights corresponding to the D3Q19 model as in [48] and the lattice speed of sound is $c_s = 1/\sqrt{3}$ as the stencil width and the discrete time step are set to unity. The bridge between the populations and the macroscopic entities of the NSE is the statistical moments over the populations or their variants, such as

$$\rho = \sum_{i=0}^{19} f_i, \tag{8}$$

$$\boldsymbol{u} = \frac{1}{\rho}\sum_{i=0}^{19} \xi_i f_i, \tag{9}$$

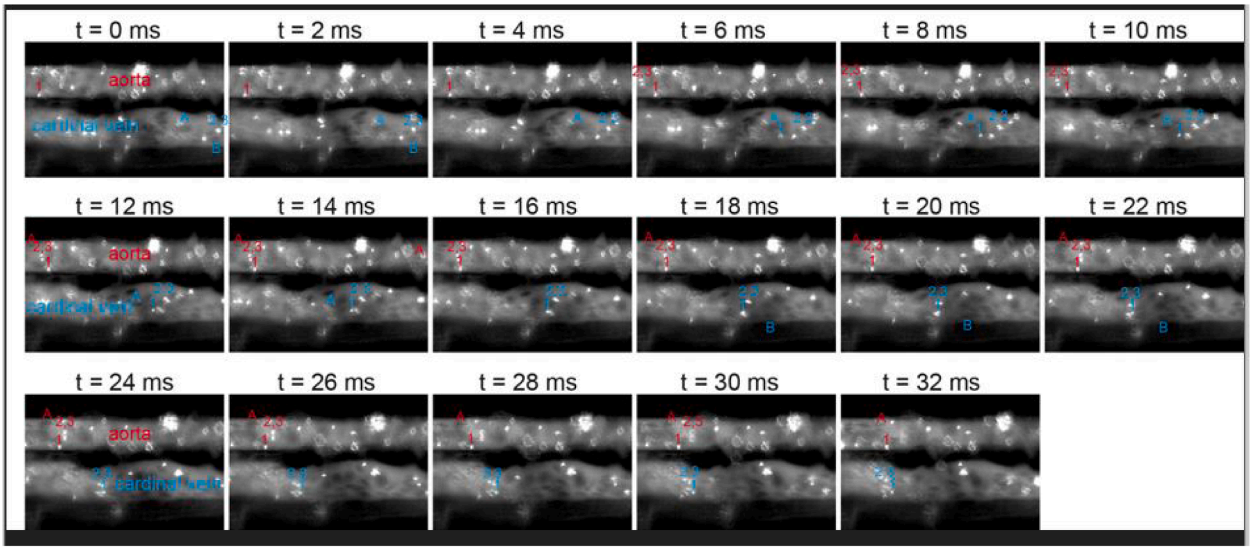

Fig. 5. Representative snapshots of a representative movie (>2000 frames) in the trunk region of a four dpf zebrafish larvae, illustrating the motion of QDots (bright dots, numbers) and erythrocytes (dark areas, letters) in the dorsal aorta (red) and the posterior cardinal vein (blue). (For interpretation of the references to colour in this figure legend, the reader is referred to the web version of this article.)

$$\triangle p = {c_s}^2 (\rho - \rho_{\text{ref}}). \tag{10}$$

Here, ρ_{ref} represents a reference pressure level converted to a density to specify the pressure from the computed pressure drop. Finally, the relaxation time is connected to the viscosity in the case of a Newtonian fluid in (6) over

$$\nu = {c_s}^2 \left(\tau - \frac{\triangle t}{2} \right). \tag{11}$$

In case of a power-law fluid, the relaxation time is computed locally from the apparent viscosity of (5), where the shear rate $\dot{\gamma}$ is approximated by the non-equilibrium parts of the populations following [14]. By applying diffusive scaling $\triangle t \propto \triangle x^2$, second-order convergence of the scheme (6) towards the incompressible forced NSE is ensured [40]. In all the numerical experiments conducted in this work, diffusive scaling is applied.

All flow simulations conducted are performed in *OpenLB* [40], an open-source C++ library for efficient LBM simulations.

3. Results

This section presents the results achieved in the conducted work. First, we present the acquisition of the input data required for the inverse problem. The parameter identification algorithm is then validated using simulated input data. Finally, the PIV-iCFD method is applied to the acquired data as a proof-of-concept.

3.1. *Data acquisition from microscopic flow images*

This section is dedicated to the data generation process that will be fed into the parameter identification process. In order to construct the digital twin of the imaged blood flow configuration, a 3D geometry model is required to bound the simulation domain in the numerical model. From the microscopic images, the velocity distribution is computed using cross-correlation.

3.1.1. *In vivo imaging of blood flow microcirculation*

To improve time resolution, we used the ZEISS Axioscope-5 to determine the flow of individual erythrocytes with a speed of up to 1 frame per ms. To visualize in parallel the flow of large specimens (erythrocytes) and small specimens (like plasma proteins) within one movie, we co-injected fluorescent QDots and Dextran-FITC in the beating embryonic heart. With this setup, we can track hundreds of individual erythrocytes and QDots, each for several time frames in one single video, see Fig. 5. In particular, the pictures in the aorta show the blood flow between two heartbeats. In addition, particles in the middle of the vessel move faster than particles in the periphery.

3.1.2. *Velocity distribution construction and vessel geometry extraction*

Before applying the cross-correlation, pre-processing of the image data is conducted to increase image quality. That is, a segmentation of the particles from the background noise and an adaptive masking to distinguish flow and non-flow regions in the image data

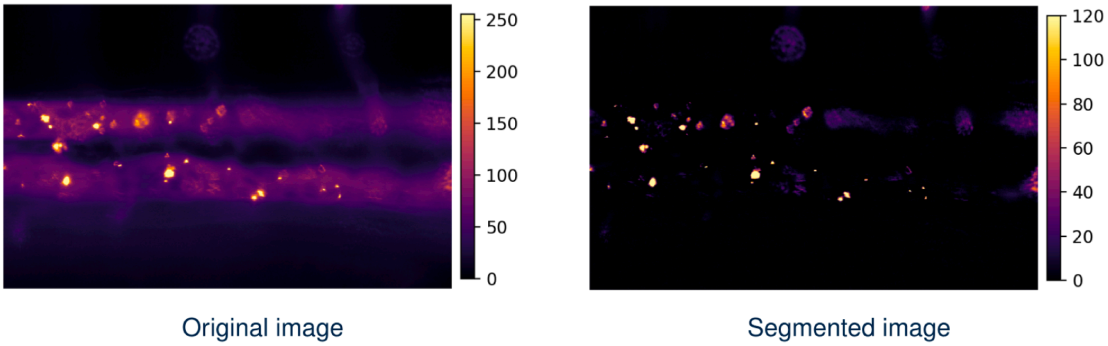

Fig. 6. Particle segmentation based on the H-dome transformation [50].

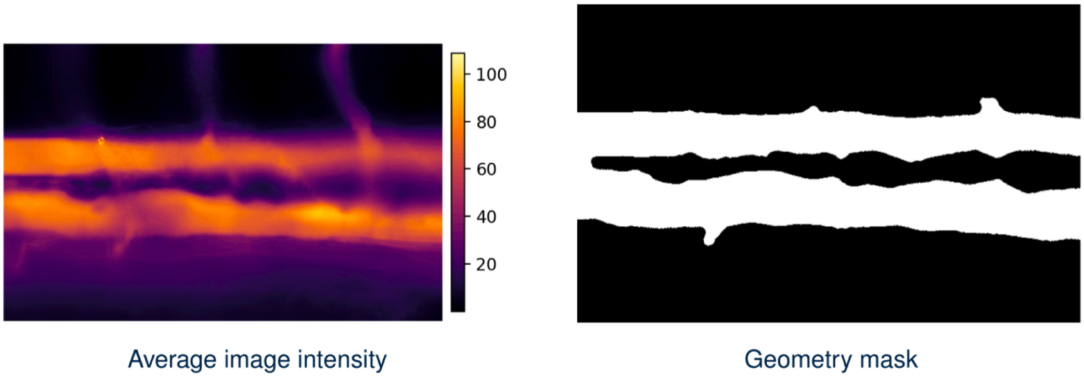

Fig. 7. Flow domain segmentation based on temporal averaged image intensity. The high intensity of the particles is used to identify flow regions.

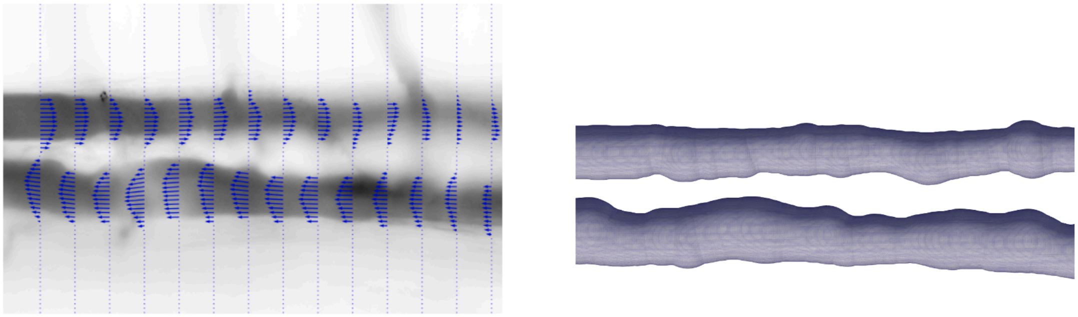

(a) Constructed velocity distribution from microscopic image data via cross-correlation.

(b) Triangulated vessel geometry representation created from the geometry mask using *PolNet* [38]. The ends of the vessels are cut to have a straight inlet and outlet required to set boundary conditions.

Fig. 8. Computed velocity distribution and vessel surface model used to construct the digital twin of the blood flow configuration from the microscopic images.

are applied. Segmentation is based on the H-dome transformation [50], where Fig. 6 shows the results for a single frame before and after segmentation.

To suppress non-zero velocities outside the flow region, an image-intensity-based masking approach is applied, where a geometry masking is computed by evaluating the image intensity averaged over the temporal scale. That is, after particle segmentation, the particles show high image intensities compared to the background, which, after averaging, shows the region that is relevant for velocity reconstruction. Then, via a threshold, a binary geometry mask is extracted. Fig. 7 shows the masking obtained from the time-averaged image.

Finally, the pre-processed image data is inserted into the PIV analysis, and the flow velocity distribution is reconstructed as shown in Fig. 8a. It can be observed that the flow velocity outside the vessels is vanishing and the flow profile inside is reconstructed with a solid radial resolution (≈ 10 probes along the diameter). Note that the distribution in Fig. 8a is the result of temporal averaging over all constructed velocity distributions per two consecutive pairs of frames. This way, velocity artifacts are reduced, and the pulsatile effects of the blood flow can be neglected. The signal intensity of the traced particles strongly affects the results, as areas with weak signal or low particle flux rates have less velocity contributions in the positive flow direction (over all frames of the movie), such that the averaging decreases the velocity in those regions. This becomes an issue if, for example, the vessel goes out of the focal plane during the imaging such that the region outside of the focal plane becomes blurry, reducing the signal intensity in that area (cf. top right region in Fig. 8a).

Using the geometry mask from Fig. 7, a three-dimensional geometry representation in the STL format is created using *PolNet* as shown in Fig. 8b. Each end of the vessels is cut to obtain clean, straight inlets and outlets, which are required to prescribe boundary conditions in the fluid simulation later. To ensure a pair of matching velocity distribution and geometry model in the inverse problem, the geometry model is extracted from the velocity-magnitude-based masking.

3.2. Inverse viscosity model parameter identification using artificial input data

This section presents the performed validation study of the parameter identification framework. In the first step, the input velocity distributions are simulated directly without involving any PIV analysis. In order to validate and investigate the formulated inverse problem, a parameter study is conducted in which simulated velocity data are used as the reference velocity. That is, for known viscosity model parameters (referred to as reference parameters), the corresponding velocity distribution is simulated, which is used as the input for the optimization framework. Then, by comparing the identified viscosity model parameters with the reference parameters, the solver can be validated regarding the accuracy of the recovered parameters, but also by varying the initial guess in the inverse problem, the robustness can be evaluated. Note that the simulation setups in the reference simulation and during the parameter identification process are identical except for the viscosity model parameters, i.e., they have the same spatial discretization, boundary conditions, etc. Thus, we can neglect common error sources, such as interpolation errors, boundary influences, and discretization errors, making this configuration suitable for validation and quality assessment. This artificial setup can be configured flexibly, allowing a better understanding and identification of the ideal operating conditions for the inverse problem. The relative error in the velocity distribution is computed by using the L^2-norm evaluated on the data points on which the reference velocity data exist.

$$\|\Delta \boldsymbol{u}\|^{\mathrm{rel}}_{L^2(\Omega^*)} = \sqrt{\frac{\sum_{\boldsymbol{x}\in\Omega^*}(\boldsymbol{u}^* - \boldsymbol{u})^2}{\sum_{\boldsymbol{x}\in\Omega^*}\boldsymbol{u}^{*2}}}. \tag{12}$$

The influence of the vessel geometry on the solvability of the inverse problem is addressed in Section 3.2.1. Then, a parameter study is conducted in Section 3.2.2 to further study the inverse problem and to illustrate the various influences.

In Section 3.2.3, an animation of particles transported by fluid flow is recorded by simulating a flow simulation containing particles. The recorded frames from the animation are inserted into the PIV algorithm to compute the velocity distribution, which is then passed as the input for the parameter identification framework. In the numerical experiments in this section, we consider the Newtonian and power-law viscosity models, where for the latter the exponent and consistency index are identified simultaneously. If not stated differently, the parameter identification algorithm uses reference velocity data of the entire flow domain Ω as input for the inverse problem. For all computed vessel geometries, the inflow diameter of $2\mathrm{m}$ is used as the characteristic length with a maximum inflow velocity of $1.0\ \mathrm{m/s}$, resulting in a Reynolds number of $\mathrm{Re} = 14.3$. The relaxation time is set to $\tau = 0.55$, and $40\ \mathrm{s}$ physical time is simulated to achieve a steady solution. For the boundary conditions, a Power-flow profile at the inlet, a pressure value at the outlet, and a no-slip treatment at the curved walls of the vessel [51] are prescribed. All the following numerical investigations are performed on a local workstation on a single GPU.

3.2.1. Simulated reference velocity distributions: Influence of the vessel geometry

The velocity profile of a Newtonian fluid in a circular pipe in cylindrical coordinates is given as

$$\boldsymbol{u}(r) = \boldsymbol{u}_{\max}(R^2 - r^2), \tag{13}$$

where R is the radius of the pipe and $\mathbf{u}_{\max}$ is the maximum velocity, which depends on the fluid viscosity ν and the pressure drop ∇p over the Hagen-Poiseuille law [48], written as

$$\boldsymbol{u}_{\max} = \frac{\rho}{4\nu}\nabla p. \tag{14}$$

One can easily see that for the setup of the inverse problem, where the inflow velocity and outlet pressure level are set in the simulation, the viscosity can not be recovered solely from the velocity field. That is, as the $\boldsymbol{u}_{\max}$ is set at the inflow, the velocity profile is fixed and only the pressure drop over the straight pipe changes for different viscosity values over the relation in (14).

Replacing the viscosity model with the power-law model, the velocity profile for the straight pipe is given as

$$\boldsymbol{u}(r) = \boldsymbol{u}_{\max}(R^{\frac{n+1}{n}} - r^{\frac{n+1}{n}}), \tag{15}$$

where $\boldsymbol{u}_{\max}$ is now given as

$$\boldsymbol{u}_{\max} = \frac{n}{n+1}\left(\frac{\rho}{2m}\nabla p\right)^{\frac{1}{n}}. \tag{16}$$

Here we can observe that the shape of the velocity profile only depends on the power-law exponent but not on the consistency index. To specify if the shape of the velocity profile depends on a parameter, one can simply compute the partial derivative of the velocity

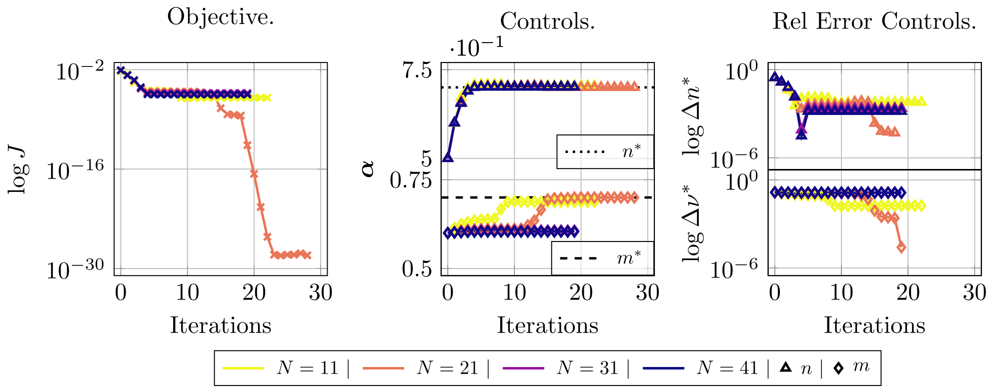

Fig. 9. Grid convergence study for the straight pipe geometry with the power-law model. For the higher resolutions, the inverse problem fails to recover the consistency index.

Fig. 10. Domains of interest (DoIs) implemented in *OpenLB* for synthetic investigations regarding the parameter identification framework. From left to right: straight pipe, 90°-bended pipe, U-shaped pipe, bifurcation.

profile with respect to the parameter. If the derivative contains the original velocity profile and is only different by a factor as it is the case for $\partial u/\partial \nu$ in (13) and for $\partial u/\partial m$ in (15), the inverse problem in the configuration as described above will not be able to recover the parameters from the velocity profile. To support this, we conducted a numerical experiment for the straight pipe with the power-law model for different grid resolutions.

In Fig. 9, the reference parameters $\boldsymbol{\alpha}^* = \{n^*, m^*\}$ are given as $n^* = 0.7$ and $m^* = 0.07\,\mathrm{m}^2/\mathrm{s}$ with an initial guess of $n^0 = 0.5$ and $m^0 = 0.06\,\mathrm{m}^2/\mathrm{s}$, corresponding to an initial relative error of 28.6% and 14.3%, respectively. Resolutions of $N = \{11, 21, 31, 41\}$ are computed, where for all resolutions the power-law index is successfully recovered with a relative final error of $\approx 10^{-3}$. However, for the higher two resolutions, the optimization algorithm fails to recover the consistency index, which aligns with our expectation for this case. The successful identification of the consistency index for the lower resolutions is due to numerical artifacts caused in the outlet region by the low resolution, which vanish for the finer mesh.

Now, the fluid flow motion in curved vessel geometries does depend on the viscosity in a way such that the shape of the velocity profile varies. This can be demonstrated by following the derivation from [52,53] regarding the analytical solution for the velocity profile in curved pipe geometries. That is, for the three-dimensional case, the velocity components are expanded by the Dean number Dn as

$$u(r,\theta) = u_0(r,\theta) + u_1(r,\theta)\mathrm{Dn} + u_2(r,\theta)\mathrm{Dn}^2 + \cdots, \tag{17}$$

$$v(r,\theta) = 0 + v_1(r,\theta)\mathrm{Dn} + v_2(r,\theta)\mathrm{Dn}^2 + \cdots, \tag{18}$$

$$w(r,\theta) = 0 + w_1(r,\theta)\mathrm{Dn} + w_2(r,\theta)\mathrm{Dn}^2 + \cdots, \tag{19}$$

where u is the velocity component in the main flow direction along the pipe centerline, v the velocity component normal to u, w the velocity component binormal to u and v. Following [52,53], steady-state fully-developed flow with constant curvature is assumed, such that the velocity profile remains constant for every cross-section perpendicular to the centerline. Therefore, the velocity components only depend on the polar coordinates in the cross-section by the radius r and the angle θ. The velocity components are expanded by the Dean number Dn, which accounts for secondary flows caused by the centrifugal force in pipe flows given as

$$\mathrm{Dn} = \mathrm{Re}\sqrt{\frac{R}{R_c}}, \tag{20}$$

where R_c is the radius of the curvature. As $\mathrm{Dn} \propto \nu^{-1}$ and thus the higher velocity terms in (19) depend on the viscosity in a non-linear fashion, the shape of the velocity is dependent on the viscosity, even under the simplified assumption of the flow being fully developed.

As a sanity check, we simulated the flow in a U-shaped curved pipe vessel geometry as shown in Fig. 10 with the Newtonian viscosity model for $\nu \in \{0.03, 0.05, 0.07\}$. For the steady-state solution, Fig. 11 shows the velocity profile along the curvature-normal

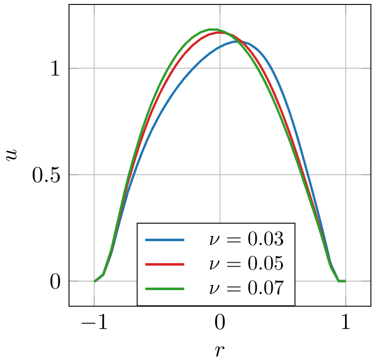

Fig. 11. Velocity profile along the curvature-normal direction in the cross-section at exactly half of the curvature, i.e., at 90° bend for the U-shaped pipe flow. The Newtonian viscosity model is used.

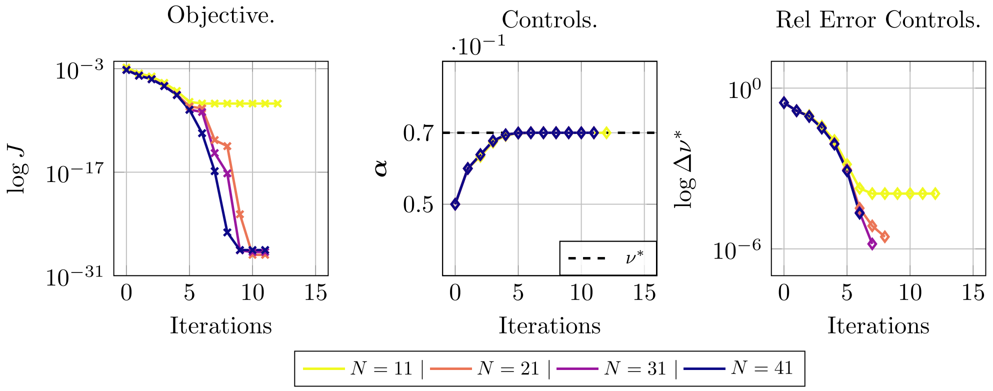

Fig. 12. Grid convergence study for the U-shaped pipe geometry with the Newtonian viscosity model. For better visualization, computed errors close to zero are omitted in the right plot.

direction in the cross-section at exactly half of the curvature, i.e., at a 90° bend. Note that for the chosen geometry, the flow is not fully developed as assumed in the derivation. Nevertheless, the dependency of the velocity profile shape on the viscosity is demonstrated, which is a necessary requirement for reconstructing the viscosity from the velocity profile in the inverse setup.

Next, the viscosity has been recovered for the Newtonian viscosity model and curved pipe geometry, where the reference viscosity is set to $\nu^* = 0.07$ with the initial control set to $\nu^* = 0.05$.

For all grid resolutions, the viscosity has been successfully recovered as shown in Fig. 12. Next, a grid convergence study is conducted for the U-shaped pipe for the power-law viscosity model. Both the power-law index and the consistency index are successfully identified by solving the inverse problem for the higher two grid resolutions as illustrated in Fig. 13. For the highest resolution, the identified parameters achieved perfect alignment with the reference parameters after 11 optimization iterations, i.e., the parameters are identified up to machine precision accuracy. This matches our expectations that the curved geometry makes the consistency index sensitive to the inverse problem.

Finally, the influence of the geometrical shape of the vessel on the inverse problem is investigated. Therein, the above illustrated four DoIs (cf. Fig. 10) are investigated for the power-law viscosity model. Fig. 14 shows the different optimization paths depending on the shape of the geometry, while the least correct results are obtained for the straight pipe and the most accurate parameters are identified for the U-shaped pipe scenario. For the straight pipe case, the consistency index is not recoverable by the inverse problem, as already observed in the grid convergence study in Fig. 9. The L-shaped pipe and bifurcation pipe yielded similar final objective values, where the bifurcation case showed a faster approach of the parameters towards their reference value. Only the U-shaped pipe and the bifurcation case can exactly recover the reference parameters.

Thus, from this point on, we focus only on the U-shaped pipe geometry for our investigations.

3.2.2. Simulated reference velocity distributions: Parameter study

This section investigates the inverse problem for the fixed resolution of $N = 31$ for the U-shaped vessel geometry regarding the following aspects:

- inflow fluid velocity,
- uncertainty in the input data,
- different initial guess for the control parameter,

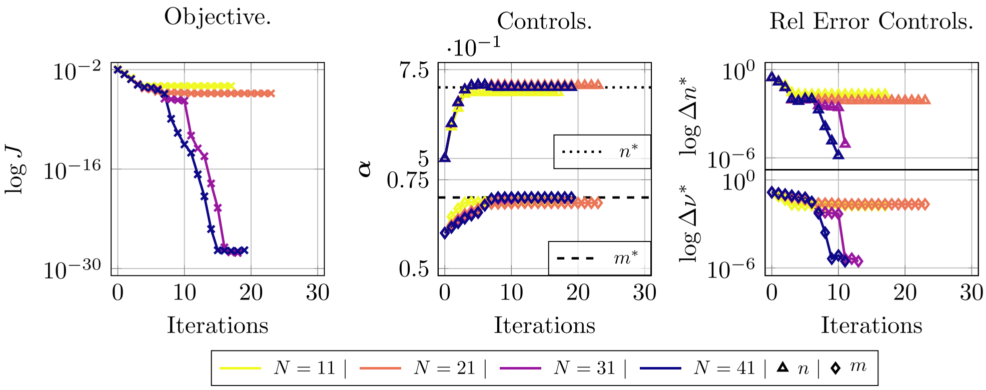

Fig. 13. Grid convergence study for the U-shaped pipe geometry with the power-law model. For the higher resolutions, the inverse problem successfully recovers both model parameters. For better visualization, computed errors close to zero are omitted in the right plot.

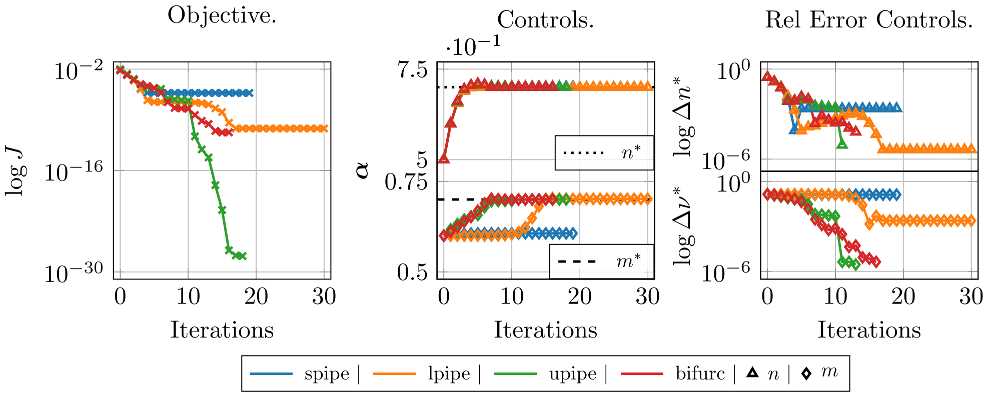

Fig. 14. Influence of the vessel geometry on the parameter identification process for the power-law model. For the straight pipe, the consistency index failed to be identified, while for the L-shaped pipe, bifurcated pipe, and U-shaped pipe, it succeeded in recovering both model parameters. Notably, machine precision is achieved for the U-shaped pipe regarding the identified parameters. For better visualization, computed errors close to zero are omitted in the right plot.

- different pressure levels,
- and the dimension of the input data.

The same reference parameters are chosen as in the previous section for the viscosity model parameters.

Flow velocity. The maximal inflow velocity ranging from $\boldsymbol{u}_{\text{in}} = \{0.1, 0.5, 1.0, 1.5, 2.0\}$ in m/s corresponding to Reynolds numbers approximately between 1.43 and 28.6 is compared. Fig. 15 presents the results for the Newtonian viscosity model, where in all cases the viscosity is recovered in the inverse problem. Fig. 16 shows the results obtained for the power-law model. Besides the lowest velocity, in all cases, the consistency index is recovered with perfect alignment (machine precision accuracy) with the corresponding reference value. It can be seen that for higher inflow velocity, the sensitivity of the inverse problem with respect to the consistency index increases, as in Fig. 16 in the middle plot, the parameter approaches the reference value with fewer iterations for increasing the inflow velocity. Notably, for the lowest velocity in Fig. 16, our method did not manage to recover the consistency index, which correlates with the observations obtained from the analytical solution. That is, the inverse problem becomes more sensitive with increasing Dean number, which is proportional to the maximum inflow velocity for the U-shaped pipe geometry. Besides the trivial case with a zero-velocity solution, this suggests the existence of a lower threshold for the Reynolds number (or the Dean number) in order to recover both power-law parameters from the velocity distribution.

Artificial noise signals. As a preparation for testing the entire workflow, additional numerical experiments are conducted to imitate realistic input data sets for the inverse problem. That is, Gaussian-distributed artificial noise signals are imposed onto the simulated reference velocity data to imitate errors produced in the input velocity data, e.g., by the cross-correlation or noise signals in the imaging. Different signal-to-noise ratios (SNR) are tested for both viscosity models, where, for all velocity components, noise signals are imposed. As expected, better results are achieved for higher SNR, but even for an SNR of 1, both viscosity model parameters are recovered with an accuracy of $< 1\%$ relative error compared to their reference values, as shown in Figs. 17 and 18. These results show the robustness of the presented approach in the presence of spatially homogeneous error sources, such as noise signals. This robustness

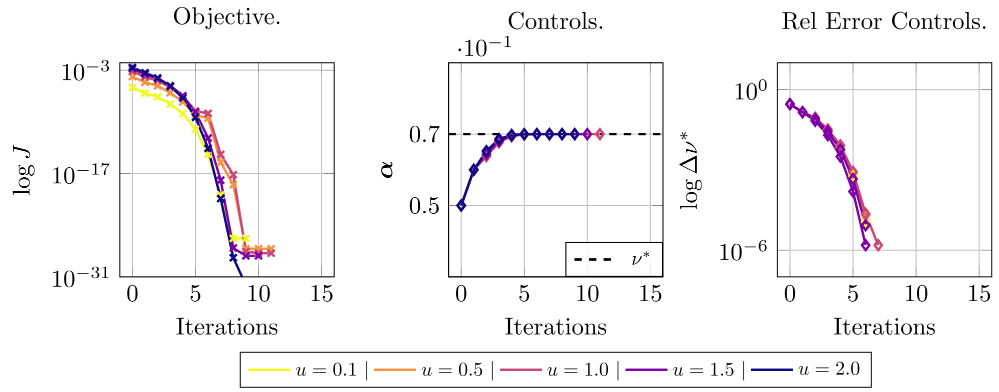

Fig. 15. Influence of the inflow velocity on the parameter identification process for the Newtonian viscosity model. For better visualization, computed errors close to zero are omitted in the right plot.

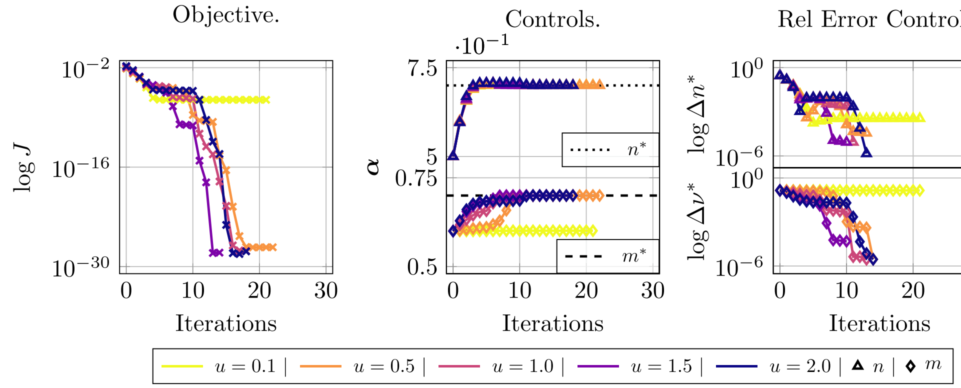

Fig. 16. Influence of the inflow velocity on the parameter identification process for the power-law viscosity model. For better visualization, computed errors close to zero are omitted in the right plot.

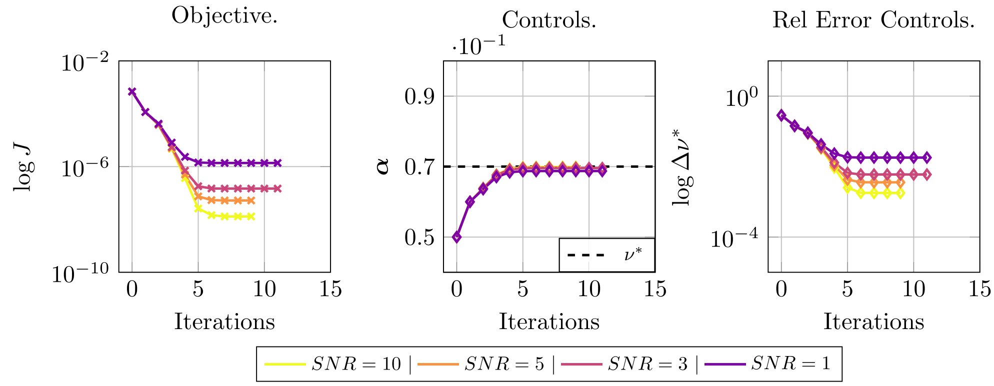

Fig. 17. Influence of noise signals imposed on the input velocity data on the parameter identification process for the Newtonian viscosity model. Different SNRs are tested.

is likely due to the high ratio of input and output values in the inverse problem, meaning that few viscosity model parameters are fitted by considering thousands of velocity values.

Initial control values. To show further the robustness of the approach, different initial control values are chosen in the inverse problem. The reference parameter is kept the same, while for the Newtonian model initial viscosity values of $\nu^0 \in \{0.05, 0.1, 0.15\}$ and for the power-law model tuples of $(n^0, m^0) \in \{(0.3, 0.05), (0.3, 0.07), (0.7, 0.09), (1.0, 0.1)\}$ are tested. For both models, Figs. 19 and 20 demonstrate the robust working of the inverse viscosity model parameter recovery.

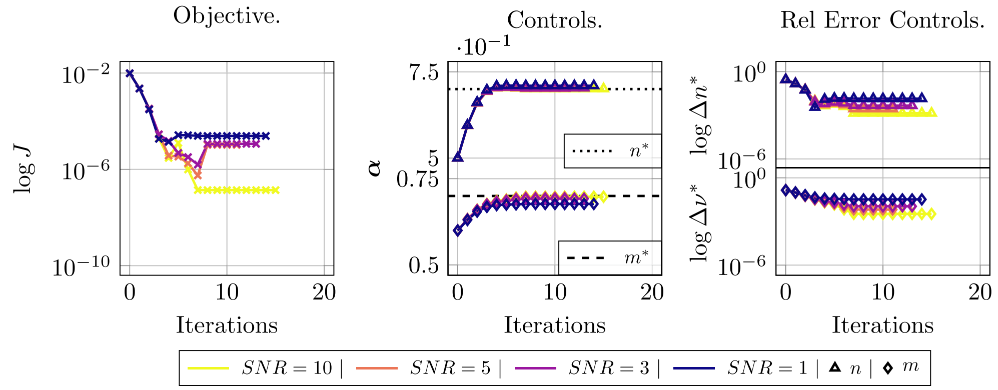

Fig. 18. Influence of noise signals imposed on the input velocity data on the parameter identification process for the power-law model. Different SNRs are tested.

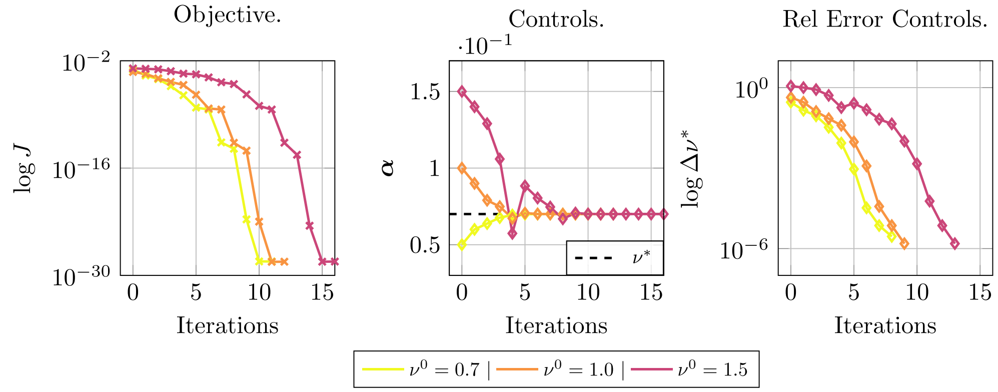

Fig. 19. Influence of the initial control on the parameter identification process for the Newtonian viscosity model.

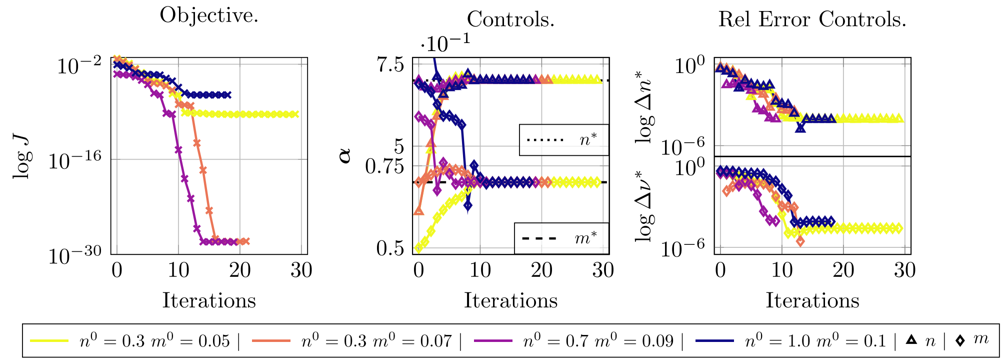

Fig. 20. Influence of the initial control on the parameter identification process for the power-law model.

Pressure level. So far, no focus has been given on the influence of the pressure on the inverse problem. As described above, the pressure level is set by the pressure boundary condition at the outlet. As the approximated incompressible Navier-Stokes equations only solve for the pressure drop, the pressure level does not influence the velocity field. In the previous section, we demonstrated the dependence of the velocity field on the viscosity for curved pipe geometries. Therefore, for a viscosity value, we obtain a corresponding velocity and pressure solution by the optimization constraints. As the pressure level is fixed by the outlet pressure, the pressure drop changes for different viscosity values. That is, the viscosity model parameter identification should work independently of the actual pressure level and solely based on the velocity distributions. To demonstrate this, we set different pressure levels by the pressure outlet condition in the reference simulation and in the simulations during the optimization, i.e., $p *= 0.4238$ bar and $p = 2p^*$, respectively. Fig. 21 shows the correct recovery of the power-law model parameters for different grid resolutions. This property is useful when real measurement data is involved, as later in Section 3.3, where the pressure level is not measurable or simply unknown.

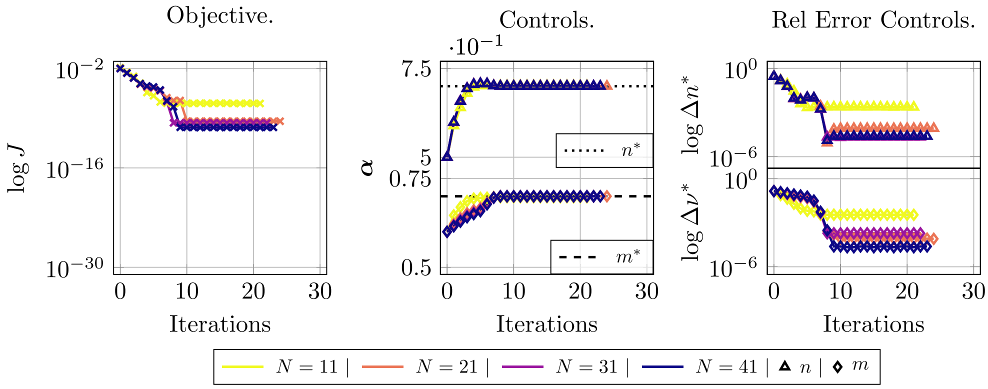

Fig. 21. Influence of the pressure level on the parameter identification process for the power-law model. During optimization, the pressure level is set to double the level from the input simulation data. The results demonstrate the correct identification of the parameters across different grid resolutions.

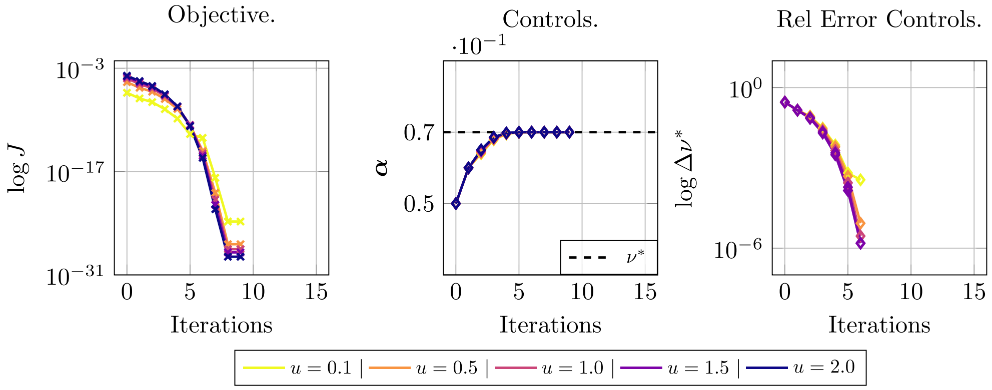

Fig. 22. Influence of the dimension of the input velocity data on the parameter identification process for the U-shaped pipe geometry and Newtonian viscosity model. Different inflow velocities are compared. For better visualization, computed errors close to zero are omitted in the right plot.

Two-dimensional input data. Finally, as the output of the cross-correlation is two-dimensional (there are also approaches for PIV allowing us to produce three-dimensional velocity distributions, but due to software restrictions of *OpenPIV*, this was not considered in this study), the reduction of the simulated input data to a two-dimensional plane is analyzed. This drastically reduces the number of input velocity values for the inverse problem. Thus, the input data are reduced from all simulation grid positions available with their velocity vectors to only those that are on the two-dimensional plane along the maximal inflow direction. Note that the velocity vectors in the close vicinity of the plane are interpolated for objective evaluation, and it is not an orthogonal projection of all the velocities onto the plane. Figs. 22 and 23 show the results for the Newtonian and power-law fluid with the same investigation as in Fig. 16, where the influence of the maximal inflow velocity is studied. For the Newtonian model, no major differences are observed. However, for the power-law model, in addition to the lowest flow velocity, the accuracy and recovery speed measured in required iterations are increasing for higher velocities. This presents a difference from the observed results in Fig. 16, where it did not yield the best results for the highest velocity. This supports the above-mentioned assumption that the asymmetry in the velocity profile strongly affects the overall parameter identification quality because the reduction of the input data increases the weight of the asymmetrical flow profile. Not only has it been shown that the inverse problem recovers the model parameters with fewer input data points, but it has also improved the accuracy and convergence speed. That is likely due to the choice of less but more sensitive input data for the inverse problem.

To summarize, the U-shaped pipe geometry with a maximum inflow velocity of at least $0.5\ \mathrm{m/s}$ or higher at the grid resolution of at least $N = 31$ currently shows the best results regarding the accuracy of the recovered parameters. It recovers even for an SNR of 1 the power-law fluid parameters up to 1% accuracy, and the algorithm operates fine even for reduced two-dimensional input velocity data. Notably, in all cases, the convergence speed of the optimization process is satisfying, as after 20 optimization steps, most of the problems converged, meaning that after 20 CFD simulations, both of the viscosity model parameters can be calculated.

3.2.3. *Constructed velocity distributions from particle transport simulations*

As the next validation step, the last two steps of the workflow in Fig. 1 are fed with an artificial movie that is produced using flow simulations with particles transported by the fluid motion. In this way, several configurations regarding the flow and therein

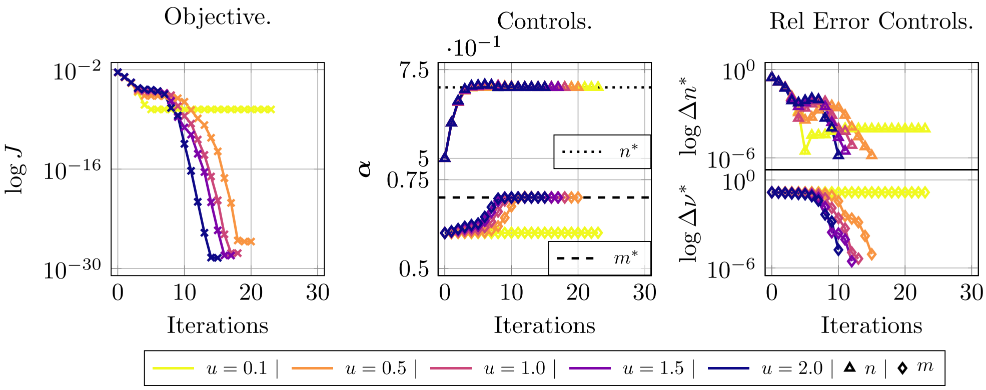

Fig. 23. Influence of the dimension of the input velocity data on the parameter identification process for the U-shaped pipe geometry and power-law model. Different inflow velocities are compared. For better visualization, computed errors close to zero are omitted in the right plot.

advected particles can be investigated, and the performance of the parameter identification framework can be assessed for velocity data input, which is constructed via cross-correlation. Similarly to the section before, by comparing the viscosity found by the inverse problem with the reference value used in the simulation to produce the artificial movie, the accuracy of the model parameters can be quantified. The particles in the reference simulation act as tracer particles for the following PIV analysis and are passively advected by the flow field [54] such that

$$\boldsymbol{v}(t) := \boldsymbol{u}(\boldsymbol{r}(t), t), \tag{21}$$

where $\boldsymbol{v} : \Omega \to \mathbf{R}^3$ is the particle velocity and $\boldsymbol{r} \in \Omega$ the particle position, where the identical time discretization is chosen as in the fluid simulation. Zeroth-order interpolation has been applied to set the flow velocity as the particle velocity. In this way, the particle position is updated via

$$\boldsymbol{r}(t + \triangle t) = \boldsymbol{r}(t) + \boldsymbol{v}(t)\triangle t. \tag{22}$$

Although in our study, we used the simplest model for passive particle transport above, advanced models such as the Verlet particle model [54] could also be applied. In the reference simulation, the U-shaped pipe in Fig. 10 is used for the reference simulation with a spatial resolution of $N = 11$ for the inflow diameter. The simulation parameters are otherwise identical to above, in addition to the inflow velocity, which is set to $\boldsymbol{u}_{\text{in}} = 1.0\text{m/s}$. The tracer particles are initialized every few discrete time steps at randomized positions in the inflow region within a bounding box of 2 cell layers. The particle flux is set to 750 particles introduced every 0.1s time step. In order to achieve a sufficient particle concentration over the entire flow domain as well as a quasi-steady state in the particulated flow, first, the flow field without particles is simulated for 40s. Then, the particles are initialized for 10 s to spread the particles through the flow domain, followed by 20 s where image frames are exported for the PIV analysis. Then, at evenly distributed time intervals of 0.2 s, simulation data is dumped at two consecutive time steps with a temporal distance of 0.008 s, which are used for the correlation. An automated Python-based *ParaView* pipeline is constructed to generate image frames from simulation data, where only particles in a specified window (cf. Fig. 24) are rendered to suppress depth-wise overlap effects in *ParaView* [55]. That is, only those particles moving inside the red box and having a maximal distance of 0.1 cm from the center in the depth direction are captured during the rendering. If the rendering window is not limited in the depth-wise direction, the in-depth particle velocities show significant discrepancies, as those moving close to the wall are reducing the overall computed velocity magnitude during correlation. In addition, the rendered area is placed in the bulk of the flow field to improve the quality of the PIV-constructed velocity distributions, as huge errors arise in the boundary region due to the lower presence of particles.

The velocity distribution computed through cross-correlation required for the inverse problem yields a relative error of $\|\Delta \boldsymbol{u}\|^{\text{rel}}_{L^2(\Omega^*)} = 5.7\%$ compared to the reference velocity distribution. Here, the maximum inflow velocity of $\boldsymbol{u}_{\text{in}} = 1.0$ m/s is set to balance the particle migration effects in the pipe curvature, leading to higher errors in the PIV analysis and the sensitivity of the consistency index in the inverse problem as observed in the study above. Fig. 24 visualizes the computed velocity distribution as blue vector arrows, which are then used for the inverse parameter identification process.

The inverse problem is first solved for the Newtonian model for different initial control values to identify the viscosity. Fig. 25 shows that for all initial controls the viscosity can be recovered. Next, the inverse problem is first solved for the power-law index and consistency index separately, identifying single-model parameters at a time. The remaining parameter has been set to the reference value. Again, the model parameters can be identified for different initial control values as shown in Figs. 26 and 27. Finally, the simultaneous identification of the power-law parameters is investigated in Fig. 28. However, for the identification of both model parameters simultaneously, the inverse problem then terminates with a final relative error of 14% and 22% for the power-law index and consistency index, respectively. A possible reason for this is the ill-posedness of the inverse problem by the error induced in the input data due to the PIV analysis. This is indicated in Fig. 28, where the objective value and the controls first approach the correct solution in the first 5 optimization iterations, but then find a different local minima with the deviating control values. We investigated different grid resolutions and various PIV-related parameters, but the identification of both parameters simultaneously

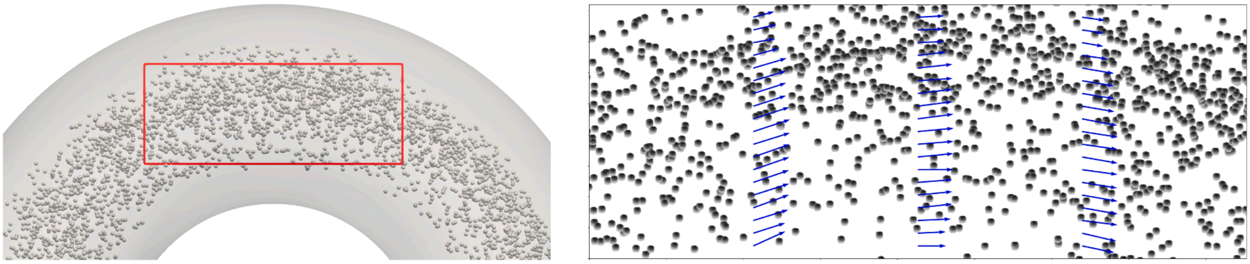

Fig. 24. Left: The highlighted region shows where particles are rendered for cross-correlation. Only those particles moving inside the red box and having a maximal distance of 0.1 cm from the center in the depth direction are captured during the rendering. Right: The computed velocity vectors with cross-correlation are visualized as blue arrows. These velocity vectors are then used in the inverse problem afterwards by interpolating the simulated velocity at those positions. (For interpretation of the references to colour in this figure legend, the reader is referred to the web version of this article.)

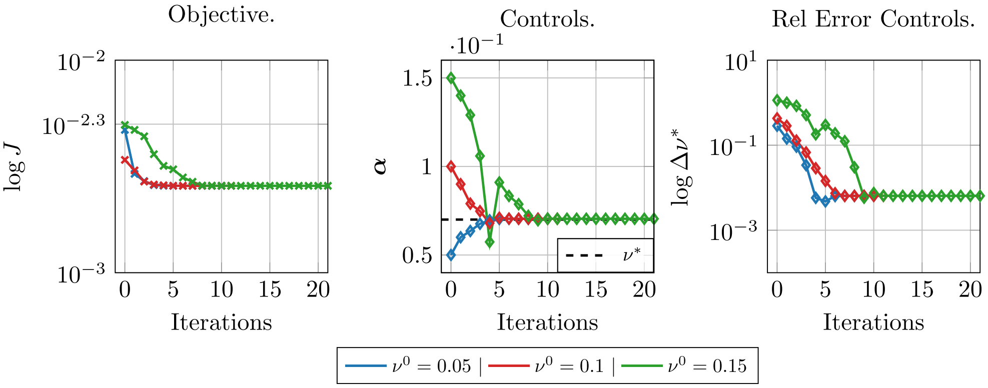

Fig. 25. Parameter identification from velocity input data constructed via PIV for the Newtonian viscosity model. Particulate flow simulation was conducted to produce image frames that are correlated to compute the velocity distribution.

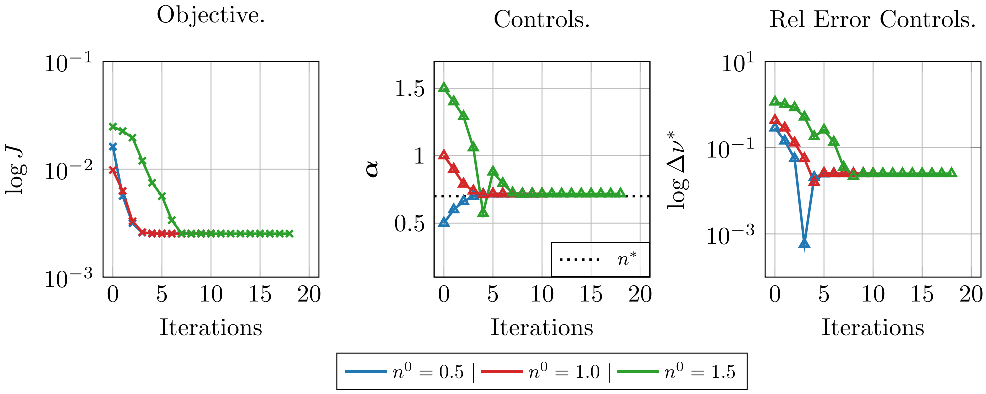

Fig. 26. Parameter identification from velocity input data constructed via PIV for the power-law exponent. Particulate flow simulation was conducted to produce image frames that are correlated to compute the velocity distribution.

remains difficult, so we defer this aspect to future research to improve the presented approach regarding this issue. However, for single parameters, our approach successfully recovers the viscosity model parameters from constructed velocity fields via PIV for different initial control values.

3.3. Application on measured in vivo images

Finally, inverse parameter identification is applied with the velocity distribution obtained from microscopic flow images in Fig. 8a. First, a reference flow simulation is performed using a literature value for effective blood viscosity in zebrafish embryos of 1.46×10^{-6} $\mathrm{m/s^2}$ [56]. The geometry of the constructed vessel from Fig. 8b is used for the fluid bounds, whereas only the venous vessel is

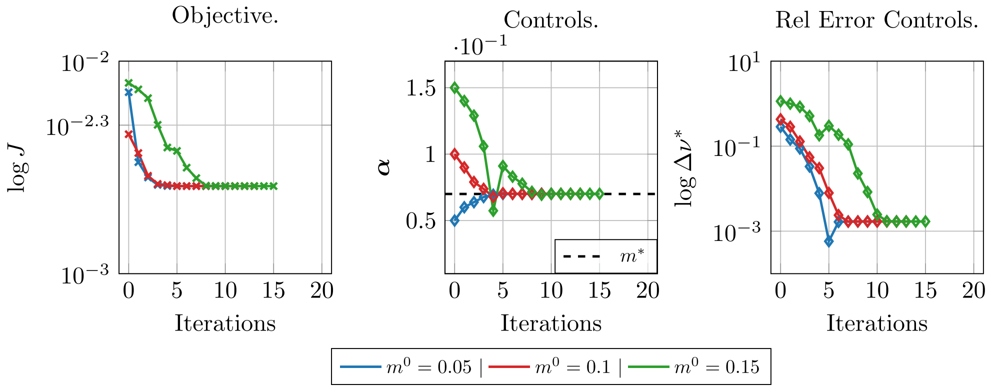

Fig. 27. Parameter identification from velocity input data constructed via PIV for the power-law consistency index. Particulate flow simulation was conducted to produce image frames that are correlated to compute the velocity distribution.

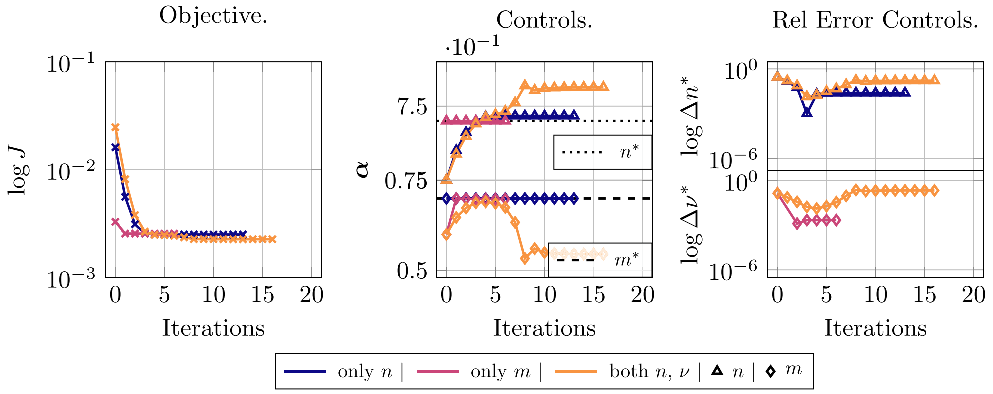

Fig. 28. Parameter identification from velocity input data constructed via PIV for both of the power-law model parameters. Particulate flow simulation was conducted to produce image frames that are correlated to compute the velocity distribution.

evaluated for error computation. That is, the velocities are averaged in the venous vessel, which shows significantly lower effects due to pulsation and the corresponding deformation of the vessel wall. However, the averaging basically neglects the pulsatile effects of the blood flow, which needs to be correctly addressed in future work by approaches accounting for this aspect, e.g., using the harmonic balance approach introduced by Koltukluo et al. [57]. At seven evenly distributed positions along the vessel, the average flow velocity over the vessel diameter is computed from the PIV results and again averaged over the seven positions to obtain an estimation of the flow rate of $u = 1.51$ mm/s. Identically, the average hydraulic vessel diameter of $D_h = 45.35$ μm for the venous blood vessel is computed from the geometry model. This produced an average Reynolds number of $Re = 0.045$ that corresponds to findings in the literature [58]. The hydraulic diameter is resolved with 31 grid positions, where at the inflow a Poiseuille flow profile and at the outflow a constant pressure is prescribed. Due to the migration of the erythrocytes in small vessels, a cell-free layer (plasma layer) in the wall vicinity is expected according to the Fåhræus-Lindqvist effect. To account for this effect, the slip condition is applied together with the Newtonian viscosity for the numerical flow model as suggested in [59–61]. By comparing the relative error, the difference between the reference simulation and the velocity distribution constructed by PIV from the microscopic images was $\|\Delta \boldsymbol{u}\|^{\mathrm{rel}}_{L^2(\Omega^*)} = 21\%$, where the errors were concentrated in the vicinity of the vessel wall. Then, the optimization problem is solved for an initial guess of the Newtonian kinetic viscosity of $\nu = 1.0 \times 10^{-6}$ m/s^2. Despite the low sensitivity of the viscosity on the velocity field that can be seen in Fig. 29 for the objective functional, the optimization framework approaches the reference value from the literature after five iterations, down to a relative error regarding the viscosity of 7%.

4. Summary and outlook

In the presented manuscript, we proposed a novel algorithm PIV-iCFD for in vivo assessment of blood viscosity from microscopic images. Cross-correlation is used to compute velocity distributions from the microscopic images, which are fed into an inverse incompressible Navier-Stokes problem solver performing iterative LBM simulations. The highlighted findings of this work are given below.

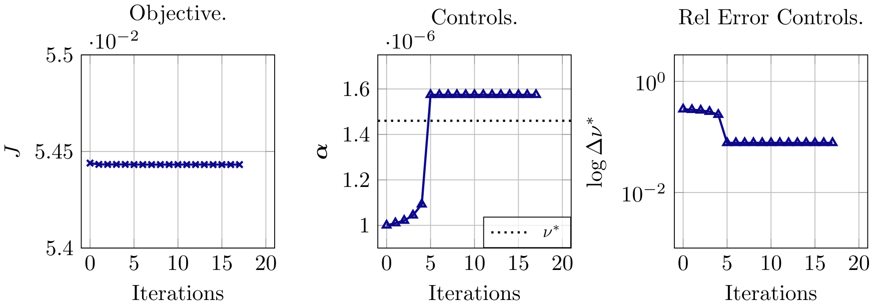

Fig. 29. Parameter identification from microscopic flow images where the velocity input data is constructed via PIV. The presence of red blood cells resulted in a plug-flow profile, which is approximated by the full slip boundary condition. (For interpretation of the references to colour in this figure legend, the reader is referred to the web version of this article.)

- Ideal operating conditions of the inverse problem are identified, i.e., viscosity model parameters for the power-law are identified up to machine precision accuracy for the curved pipe geometry for $Re \geq 5$.
- Noisy input velocity data with an SNR of 1 yielded a relative error less than 1%, demonstrating the robustness of the approach by using distributed input data
- When PIV constructed velocity data from particulate simulations are used as synthetic input, the power-law index and the consistency index are identified separately (from a velocity distribution with a relative error of 5.7% for PIV vs. CFD) up to an accuracy of 2% and 0.2%, respectively.
- Using micro-PIV on real microscopic flow images on zebrafish embryos, velocity distributions are produced for the input data, where the effective blood viscosity is found with a relative error of 7% to the reference values from the literature.
- The slip boundary treatment yielded better results than the commonly applied no-slip treatment in the effective viscosity estimation for the zebrafish embryos.

The promising results of this work motivate future research directions. In the synthetic cases, the choice of the viscosity model (here Newtonian or power-law fluid) does not yield major differences regarding the sensitivity in the inverse problem.

The results obtained present a proof-of-concept and need to be further investigated. That is, the overall low sensitivity of the kinematic viscosity on the velocity profile is due to the ill-posed inverse problem, as shown in the synthetic analysis with the straight vessel geometry. In fact, a high sensitivity of the outcome on the initial guess could be observed for this case, emphasizing the current problem. As good results regarding the robustness of the parameter identification problem are obtained for a non-straight vessel geometry in the artificial case, the next study should target vessel geometries with curvatures, as that increases the sensitivity regarding the viscosity. Next, we expect that the lack of presence of erythrocytes in the numerical model, affecting the velocity profile (Poiseuille vs. Plug-flow), introduced a significant contribution to the error produced between simulation and measurement. That is, when applying no-slip boundary conditions in the simulation, the relative error increases to approximately $\|\Delta \boldsymbol{u}\|^{\mathrm{rel}}_{L^2(\Omega^*)} = 35\%$, and the optimization algorithm fails to identify the viscosity. Finally, the correct inclusion of pulsatile effects should also be addressed to account for those effects, e.g., by implementing the harmonic balance method from [57].

From the observations made in the previous studies, it is known that PIV analysis itself produces higher errors in the vicinity of the wall. Furthermore, as shown in Section 3.2.3, the quality of the PIV analysis and the underlying measurement data is essential, as errors introduced in these steps limit the successful recovery of the viscosity parameters, especially for the simultaneous recovery of multiple parameters. To address this issue, the following measures on the experimental side should be taken into account to reduce the error between simulation and measurements. First, larger vessels or a higher magnification on the blood vessel should be considered to increase the spatial resolution in the PIV analysis, allowing for focus on velocity data in the bulk of the vessel. Second, by reducing the concentration of erythrocytes through genetic modification of embryos, the assumption of a Newtonian fluid model becomes more accurate, reducing the errors produced on the wall due to the wrong boundary treatment. Furthermore, the particulate effects on the viscosity vanish, making the identified viscosity parameter more comparable to the blood plasma viscosity.

Finally, targeting larger blood vessels (diameter greater than 300 μm) allows applying macroscopic viscosity models such as power-law or Casson models that allow the identification of those model parameters that could reveal more clinically relevant information from the blood flow images.

Funding

This research was partly funded by the German Research Foundation for the project “CFD-MRI Reactions - A Combined Measurement-Simulation Approach for Reactive Flow Characterization” (grant number 517581625) and by the German Research Foundation for the project “HiResHemo: Hemodynamics at High Spatio-temporal Resolution by Comparative Visual Analysis of 4D PC-MRI Data and CFD Simulation Ensembles ” (grant number 468824876).

Ethics statement

Zebrafish husbandry and experimental procedures were performed in accordance with local and national German animal welfare standards and were approved by the government of Baden-Württemberg, Regierungspräsidium Karlsruhe, Germany (Akz.: 35–9185.64/BH KIT ZOO-ZE).

CRediT authorship contribution statement

Shota Ito: Writing – review & editing, Writing – original draft, Visualization, Validation, Software, Methodology, Investigation, Formal analysis, Data curation, Conceptualization; **Moritz Vogel:** Visualization, Validation, Software, Investigation, Formal analysis, Data curation; **Adrian A. Fessler:** Visualization, Validation, Software; **Adrian Kummerländer:** Software; **Anna Lischke:** Methodology, Data curation; **Dietmar Gradl:** Writing – review & editing, Validation, Methodology, Data curation; **Ferdinand le Noble:** Writing – review & editing, Validation, Supervision, Resources, Methodology, Funding acquisition, Conceptualization; **Mathias J. Krause:** Writing - review & editing, Supervision, Software, Resources, Methodology, Funding acquisition, Conceptualization; **Stephan Simonis:** Writing – review & editing, Supervision, Project administration, Methodology, Funding acquisition, Formal analysis, Conceptualization.

Data availability

The results in this paper were produced with open-source tools *OpenPIV* (published under the MIT license) [39] for the cross-correlation, PolNet (published under the GNU Lesser General Public License) [38] for the geometry model segmentation, *ParaView* for the frame generation in the validation pipeline (published under the permissive BSD 3-clause license), and *OpenLB* [40] (published under GNU General Public License V.2 (GPL2), version 1.8.1 [62]) for the flow simulation and solving of the inverse problem. The experimental and computational data are available upon reasonable request.

Declaration of competing interest

The authors declare that they have no known competing financial interests or personal relationships that could have appeared to influence the work reported in this paper.

Acknowledgments

The authors acknowledge support from a ZEISS Collaboration Catalyst Grant.

Supplementary material

Supplementary material associated with this article can be found in the online version at 10.1016/j.cma.2026.118927.

Appendix A.

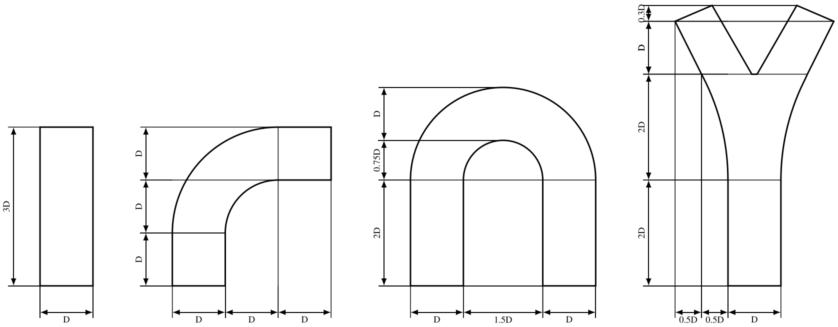

Fig. A.30. Centerline plane projection for the DoIs implemented for synthetic investigations regarding the parameter identification framework. From left to right: straight pipe, 90°-bended pipe, U-shaped pipe, bifurcation.

The synthetic vessel geometries used in Section 3.2.1 are shown in Fig. A.30 with the dimensions given corresponding to the inlet diameter D illustrated as projections onto the plane which includes the centerline of the flow path.

References

[1] M. Vaduganathan, G.A. Mensah, J.V. Turco, V. Fuster, G.A. Roth, The global burden of cardiovascular diseases and risk, JACC 80 (25) (2022) 2361–2371. https://doi.org/10.1016/j.jacc.2022.11.005

[2] G.A. Roth, C. Johnson, A. Abajobir, F. Abd-Allah, S.F. Abera, et al., Global, regional, and national burden of cardiovascular diseases for 10 causes, 1990 to 2015, JACC 70 (1) (2017) 1–25. https://doi.org/10.1016/j.jacc.2017.04.052

[3] T.G. Papaioannou, E.N. Karatzis, M. Vavuranakis, J.P. Lekakis, C. Stefanadis, Assessment of vascular wall shear stress and implications for atherosclerotic disease, Int. J. Cardiol. 113 (1) (2006) 12–18. https://doi.org/10.1016/j.ijcard.2006.03.035

[4] E. Cecchi, C. Giglioli, S. Valente, C. Lazzeri, G.F. Gensini, R. Abbate, L. Mannini, Role of hemodynamic shear stress in cardiovascular disease, Atherosclerosis 214 (2) (2011) 249–256. https://doi.org/10.1016/j.atherosclerosis.2010.09.008

[5] P. Libby, P.M. Ridker, A. Maseri, Inflammation and atherosclerosis, Circulation 105 (9) (2002) 1135–1143. https://doi.org/10.1161/hc0902.104353

[6] D. Nolte, C. Bertoglio, Inverse problems in blood flow modeling: a review, Int. J. Numer. Method Biomed. Eng. 38 (8) (2022) e3613. https://doi.org/10.1002/cnm.3613

[7] G.D. Lowe, A.J. Lee, A. Rumley, J.F. Price, F.G. Fowkes, Blood viscosity and risk of cardiovascular events: the edinburgh artery study, Br. J. Haematol. 96 (1) (1997) 168-173. https://doi.org/10.1046/j.1365-2141.1997.8532481.x

[8] W. Koenig, M. Sund, B. Filipiak, A. Döring, H. Löwel, E. Ernst, Plasma viscosity and the risk of coronary heart disease, Arterioscler. Thromb. Vasc. Biol. 18 (5) (1998) 768–772. https://doi.org/10.1161/01.ATV.18.5.768

[9] V. Kannojiya, A.K. Das, P.K. Das, Simulation of blood as fluid: a review from rheological aspects, IEEE Rev. Biomed. Eng. 14 (2021) 327–341. https://doi.org/10.1109/RBME.2020.3011182

[10] G. de Simone, R.B. Devereux, S. Chien, M.H. Alderman, S.A. Atlas, J.H. Laragh, Relation of blood viscosity to demographic and physiologic variables and to cardiovascular risk factors in apparently normal adults, Circulation 81 (1) (1990) 107–117. https://doi.org/10.1161/01.CIR.81.1.107

[11] J. Danesh, R. Collins, R. Peto, G.D.O. Lowe, Haematocrit, viscosity, erythrocyte sedimentation rate: meta-analyses of prospective studies of coronary heart disease, Eur. Heart J. 21 (7) (2000) 515–520. https://doi.org/10.1053/euhj.1999.1699

[12] J.S. Oh, P. Prabhakaran, D.K. Seo, D.Y. Kim, W. Lee, K.H. Ahn, A comparative study of blood viscometers of 3 different types, Clin. Hemorheol. Microcirc. 88 (2) (2024) 211–219. https://doi.org/10.3233/CH-242256

[13] M. Valério de Arruda, A. Cruz Silva, J.C. Fernandes Galduróz, R. Ferreira Galduróz, Standardization for obtaining blood viscosity: a systematic review, Eur. J. Haematol. 106 (5) (2021) 597–605. https://doi.org/10.1111/ejh.13594

[14] J. Boyd, J.M. Buick, S. Green, Analysis of the casson and Carreau-Yasuda non-Newtonian blood models in steady and oscillatory flows using the lattice Boltzmann method, Phys. Fluids 19 (9) (2007) 093103. https://doi.org/10.1063/1.2772250

[15] G. Li, T. Ye, B. Yang, S. Wang, X. Li, Temporal-spatial heterogeneity of hematocrit in microvascular networks, Phys. Fluids 35 (2) (2023) 021906. https://doi.org/10.1063/5.0139641

[16] P.D. Morris, A. Narracott, H. von Tengg-Kobligk, D.A. Silva Soto, S. Hsiao, A. Lungu, P. Evans, N.W. Bressloff, P.V. Lawford, D.R. Hose, J.P. Gunn, Computational fluid dynamics modelling in cardiovascular medicine, Heart 102 (1) (2016) 18–28. https://doi.org/10.1136/heartjnl-2015-308044

[17] L. Byoung-Kwon, Computational fluid dynamics in cardiovascular disease, KCJ 41 (8) (2011) 423–430. https://doi.org/10.4070/kcj.2011.41.8.423

[18] G.R. Cokelet, H.J. Meiselman, Macro-and micro-rheological properties of blood, Biomed. Health Res. Commission Eur. Communities Then IOS Press 69 (2007) 45.

[19] T. Ye, N. Phan-Thien, C.T. Lim, Particle-based simulations of red blood cells-a review, J. Biomech. 49 (11) (2016) 2255–2266. Selected Articles from the International Conference on CFD in Medicine and Biology (Albufeira, Portugal - August 30th - September 4th, 2015). https://doi.org/10.1016/j.jbiomech.2015.11.050

[20] T. Krüger, F. Varnik, D. Raabe, Efficient and accurate simulations of deformable particles immersed in a fluid using a combined immersed boundary lattice Boltzmann finite element method, Comput. Math. Appl. 61 (12) (2011) 3485–3505.

[21] Y.-H. Tang, L. Lu, H. Li, C. Evangelinos, L. Grinberg, V. Sachdeva, G.E. Karniadakis, OpenRBC: a fast simulator of red blood cells at protein resolution, Biophys. J. 112 (10) (2017) 2030–2037.

[22] F.J.H. Gijsen, F.N. van de Vosse, J.D. Janssen, The influence of the non-Newtonian properties of blood on the flow in large arteries: steady flow in a carotid bifurcation model, J. Biomech. 32 (6) (1999) 601–608. https://doi.org/10.1016/S0021-9290(99)00015-9

[23] M.A.H. Mohd Adib, S. Ii, Y. Watanabe, S. Wada, Minimizing the blood velocity differences between phase-contrast magnetic resonance imaging and computational fluid dynamics simulation in cerebral arteries and aneurysms, Med. Biol. Eng. Comput. 55 (9) (2017) 1605–1619.

[24] S.W. Funke, M. Nordaas, O. Evju, M.S. Alnæs, K.A. Mardal, Variational data assimilation for transient blood flow simulations: cerebral aneurysms as an illustrative example, Int. J. Numer. Method Biomed. Eng. 35 (1) (2019) e3152. e3152 cnm.3152. https://doi.org/10.1002/cnm.3152

[25] T.S. Koltukluoğlu, P.J. Blanco, Boundary control in computational haemodynamics, J. Fluid Mech. 847 (2018) 329–364. https://doi.org/10.1017/jfm.2018.329

[26] C.J. Arthurs, N. Xiao, P. Moireau, T. Schaeffter, C.A. Figueroa, A flexible framework for sequential estimation of model parameters in computational hemodynamics, Adv. Model. Simul. Eng. Sci. 7 (1) (2020) 48.

[27] M. Perego, A. Veneziani, C. Vergara, A variational approach for estimating the compliance of the cardiovascular tissue: an inverse fluid-structure interaction problem, SIAM J. Sci. Comput. 33 (3) (2011) 1181–1211. https://doi.org/10.1137/100808277

[28] F. Klemens, S. Schuhmann, G. Guthausen, G. Thäter, M.J. Krause, CFD-MRI: A coupled measurement and simulation approach for accurate fluid flow characterisation and domain identification, Comput. Fluids 166 (2018) 218–224. https://doi.org/10.1016/j.compfluid.2018.02.022

[29] F. Klemens, S. Schuhmann, R. Balbierer, G. Guthausen, H. Nirschl, G. Thäter, M.J. Krause, Noise reduction of flow MRI measurements using a lattice Boltzmann based topology optimisation approach, Comput. Fluids 197 (2020) 104391. https://doi.org/10.1016/j.compfluid.2019.104391

[30] A. Kontogiannis, S.V. Elgersma, A.J. Sederman, M.P. Juniper, Bayesian inverse Navier-Stokes problems: joint flow field reconstruction and parameter learning, Inverse Probl. 41 (1) (2024) 015008. https://doi.org/10.1088/1361-6420/ad9cb7

[31] K. Larson, C. Bowman, C. Papadimitriou, P. Koumoutsakos, A. Matzavinos, Detection of arterial wall abnormalities via Bayesian model selection, R. Soc. Open Sci. 6 (10) (2019) 182229. https://doi.org/10.1098/rsos.182229

[32] M. Habibi, R.M. D'Souza, S.T.M. Dawson, A. Arzani, Integrating multi-fidelity blood flow data with reduced-order data assimilation, Comput. Biol. Med. 135 (2021) 104566. https://doi.org/10.1016/j.compbiomed.2021.104566

[33] A. Kontogiannis, R. Hodgkinson, S. Reynolds, E.L. Manchester, Learning rheological parameters of non-Newtonian fluids from velocimetry data, J. Fluid Mech. 1011 (2025) R3. https://doi.org/10.1017/jfm.2025.92

[34] J.Y. Lee, H.S. Ji, S.J. Lee, Micro-PIV measurements of blood flow in extraembryonic blood vessels of chicken embryos, Physiol. Meas. 28 (10) (2007) 1149. https://doi.org/10.1088/0967-3334/28/10/002

[35] S. Ito, J. Jeßberger, S. Simonis, F. Bukreev, A. Kummerländer, A. Zimmermann, G. Thäter, G.R. Pesch, J. Thöming, M.J. Krause, Identification of reaction rate parameters from uncertain spatially distributed concentration data using gradient-based PDE constrained optimization, Comput. Math. Appl. 167 (2024) 249–263. https://doi.org/10.1016/j.camwa.2024.05.026

[36] S. Ito, S. Großmann, F. Bukreev, J. Jeßberger, M.J. Krause, Benchmark case for the inverse determination of adsorption parameters using lattice Boltzmann methods and gradient-based optimization, Chem. Eng. Sci. 309 (2025) 121467. https://doi.org/10.1016/j.ces.2025.121467

[37] A. Kummerländer, M. Dorn, M. Frank, M.J. Krause, Implicit propagation of directly addressed grids in lattice Boltzmann methods, Concurrency Comput. Pract. Exper. 35 (8) (2023) e7509. https://doi.org/10.1002/cpe.7509

[38] M.O. Bernabeu, M.L. Jones, R.W. Nash, A. Pezzarossa, P.V. Coveney, H. Gerhardt, C.A. Franco, PolNet: a tool to quantify network-level cell polarity and blood flow in vascular remodeling, Biophys. J. 114 (9) (2018) 2052–2058. https://doi.org/10.1016/j.bpj.2018.03.032

[39] H. Ben-Gida, R. Gurka, A. Liberzon, OpenPIV-MATLAB - an open-source software for particle image velocimetry; test case: birds' aerodynamics, SoftwareX 12 (2020) 100585. https://doi.org/10.1016/j.softx.2020.100585

[40] M.J. Krause, A. Kummerländer, S.J. Avis, H. Kusumaatmaja, D. Dapelo, F. Klemens, M. Gaedtke, N. Hafen, A. Mink, R. Trunk, J.E. Marquardt, M.-L. Maier, M. Haussmann, S. Simonis, OpenLB-open source lattice Boltzmann code, 2021. https://doi.org/10.1016/j.camwa.2020.04.033

[41] A.K. Jain, Fundamentals of digital image processing, Englewood Cliffs, NJ Prentice Hall (1989). https://doi.org/10.1016/0734-189X(89)90041-8

[42] D.C. Liu, J. Nocedal, On the limited memory BFGS method for large scale optimization, Math. Program. 45 (1) (1989) 503–528. https://doi.org/10.1007/BF01589116

[43] M.D. Gunzburger, Perspectives in flow control and optimization, Soc. Ind. Appl. Math. (2002). https://doi.org/10.1137/1.9780898718720

[44] A. Griewank, A. Walther, Evaluating derivatives, Soc. Ind. Appl. Math. (2008). https://doi.org/10.1137/1.9780898717761

[45] S. Simonis, Lattice Boltzmann Methods for Partial Differential Equations, Doctoral thesis, Karlsruhe Institute of Technology (KIT), 2023. https://doi.org/10.5445/IR/1000161726

[46] J. Jeßberger, J.E. Marquardt, L. Heim, J. Mangold, F. Bukreev, M.J. Krause, Optimization of a micromixer with automatic differentiation, Fluids 7 (5) (2022) 144. https://doi.org/10.3390/fluids7050144

[47] P.L. Bhatnagar, E.P. Gross, M. Krook, A model for collision processes in gases. i. small amplitude processes in charged and neutral one-component systems, Phys. Rev. 94 (3) (1954) 511–525. https://doi.org/10.1103/PhysRev.94.511

[48] T. Krüger, H. Kusumaatmaja, A. Kuzmin, O. Shardt, G. Silva, E.M. Viggen, The lattice Boltzmann method: principles and practice, Springer Int. Publ. (2017). https://doi.org/10.1007/978-3-319-44649-3

[49] Y.H. Qian, D. D'Humières, P. Lallemand, Lattice BGK models for Navier-Stokes equation, Europhys. Lett. 17 (6) (1992) 479. https://doi.org/10.1209/0295-5075/17/6/001

[50] X. Geng, A. Liu, Y. Chen, G. Meyers, The area-reconstruction h-dome technique and its efficient python implementation for improved particle size image analysis, Microsc. Res. Tech. 86 (5) (2023) 614–626. https://doi.org/10.1002/jemt.24300

[51] R. Mei, L.-S. Luo, W. Shyy, An accurate curved boundary treatment in the lattice Boltzmann method, J. Comput. Phys. 155 (2) (1999) 307–330. https://doi.org/10.1006/jcph.1999.6334

[52] W.R. Dean, J.M. Hurst, Note on the motion of fluid in a curved pipe, Mathematika 6 (1) (1959) 77–85. https://doi.org/10.1112/S0025579300001947

[53] S. Ajgoun, J.Khalid Naciri, R. Khatyr, Semi analytical method for calculating dean's vortex in torus of elliptical cross section, MATEC Web Conf. 286 (2019) 07004. https://doi.org/10.1051/matecconf/201928607004

[54] D. Frenkel, B. Smit, Understanding molecular simulation: from algorithms to applications, Elsevier (2023). https://doi.org/10.1016/B978-0-12-267351-1.X5000-7

[55] U. Ayachit, The paraview guide: a parallel visualization application, Kitware Inc. (2015). https://www.paraview.org/

[56] J. Lee, T.-C. Chou, D. Kang, H. Kang, J. Chen, K.I. Baek, W. Wang, Y. Ding, D.D. Carlo, Y.-C. Tai, et al., A rapid capillary-pressure driven micro-channel to demonstrate newtonian fluid behavior of zebrafish blood at high shear rates, Sci. Rep. 7 (1) (2017) 1980. https://doi.org/10.1038/s41598-017-02253-7

[57] T.S. Koltukluoğlu, G. Cvijetić, R. Hiptmair, Harmonic balance techniques in cardiovascular fluid mechanics, in: D. Shen, T. Liu, T.M. Peters, L.H. Staib, C. Essert, S. Zhou, P.-T. Yap, A. Khan (Eds.), Medical Image Computing and Computer Assisted Intervention – MICCAI 2019, Springer International Publishing, Cham, 2019, pp. 486–494.

[58] H. Fukui, R.W.-Y. Chow, C.H. Yap, J. Vermot, Rhythmic forces shaping the zebrafish cardiac system, Trends Cell Biol. 35 (2) (2025) 166–176. https://doi.org/10.1016/j.tcb.2024.10.012

[59] A.E. Kovtanyuk, E.A. Marushchenko, R. Lampe, The role of boundary conditions for modeling the blood flow in microvessels, in: Journal of Physics Conference Series, 2514, IOP Publishing, 2023, p. 012012.

[60] D. Hershey, S.J. Cho, Blood flow in rigid tubes: thickness and slip velocity of plasma film at the wall, J. Appl. Physiol. 21 (1) (1966) 27–32.

[61] A. Zeeshan, A. Fatima, F. Khalid, M.M. Bhatti, Interaction between blood and solid particles propagating through a capillary with slip effects, Microvasc. Res. 119 (2018) 38–46. https://doi.org/10.1016/j.mvr.2018.04.004

[62] A. Kummerländer, T. Bingert, F. Bukreev, L. E. Czelusniak, D. Dapelo, C. Gaul, N. Hafen, S. Ito, J. Jeßberger, D. Khazaeipoul, T. Krüger, H. Kusumaatmaja, J. E. Marquardt, A. Raeli, M. Rennick, F. Prinz, M. Schecher, A. Schneider, Y. Shimojima, S. Simonis, P. Sitter, P. Spelten, A. Tacques, D. Teutscher, M. Zhong, M. J. Krause, OpenLB Release 1.8.1: Open Source Lattice Boltzmann Code, Zenodo, (2025). https://doi.org/10.5281/zenodo.15440776